Influences of Mesoscale Ocean Eddies on Flow Vertical Structure in a Resolution-Based Model Hierarchy

Elizabeth Yankovsky, Laure Zanna, K. Shafer Smith [1]

[1]Courant Institute of Mathematical Sciences, New York University, New York, NY

Key Points:

- We use idealized modeling to study mesoscale eddy influences on vertical structure as a function of grid resolution and dynamical regime.
- When eddies are unresolved, particularly in weak mean flow regions, the flow fails to barotropize and energy is trapped in baroclinic modes.
- We identify scalings characterizing barotropic to baroclinic kinetic energy ratios and discuss implications for improving parameterizations.

Corresponding author: Elizabeth Yankovsky, eay8226@nyu.edu

Abstract

The understanding and representation of energetic transfers associated with ocean mesoscale eddies is fundamental to the development of parameterizations for climate models. We investigate the influence of eddies on flow vertical structure as a function of underlying dynamical regime and grid resolution. We employ the GFDL-MOM6 in an idealized configuration and systematically consider four horizontal resolutions: 1/4°, 1/8°, 1/16°, and 1/32°. We analyze the distributions of potential and kinetic energy, decomposed into barotropic and baroclinic, and eddy and mean parts. Kinetic energy increases and potential energy decreases as resolution increases and captures more baroclinically-unstable modes. The dominant trend in vertical structure is an increasing fraction of kinetic energy going into the barotropic mode, particularly its eddy component, as eddies are increasingly resolved. We attribute the increased baroclinicity at low resolutions to inaccurate representation of vertical energy fluxes, leading to suppressed barotropization and energy trapping in high vertical modes. We also explore how the underlying dynamical regime influences energetic pathways. In cases where large-scale flow is dominantly barotropic, resolving the deformation radius is less crucial to accurately capturing the flow's vertical structure. We find the barotropic kinetic energy fraction to be a useful metric in assessing vertical structure. In the highest-resolution case, the barotropic kinetic energy fraction correlates with the scale separation between the deformation scale and the energy-containing scale, i.e. the extent of the eddy-driven inverse cascade. This work suggests that mesoscale eddy parameterizations should incorporate the energetic effects of eddies on vertical structure in a scale-aware, physically-informed manner.

Plain Language Summary

Ocean eddies with scales of 10s to 100s of kilometers are highly energetic features which have a significant influence on the ocean state. Eddies are notoriously challenging to fully capture in modern climate models as they require grid resolutions finer than current computational resources allow for. Our goal is to study the effect of eddies in a simplified model. In particular, we focus on how eddies shape flow vertical structure and redistribute energy. By using a simplified model, we are able to perform high-resolution simulations where eddies are fully resolved and compare against resolutions that barely permit eddies. In the latter case, the vertical structure of the flow is adversely affected. Eddies transfer energy and information from the ocean surface to depths of thousands of meters. Under-resolving them leads to energy trapping near the surface and within small vertical scales, altering the ocean energy cycle. We also investigate the influence of the underlying flow regime; for weak and non-uniform with depth flows resolving eddies is crucial to obtaining the correct vertical structure. Our results may guide how to improve eddy representation in more complex and realistic climate models.

1 Introduction

Ocean dynamics are characterized by nonlinear interactions ranging from planetary forcing scales down to molecular scales at which frictional energy dissipation occurs. Atmospheric and radiative forcing establish the large-scale mean ocean circulation and isopycnal structure, maintaining the largest reservoir of available potential energy (APE) in the ocean. The kinetic energy (KE) of the mean circulation is ~ 1000 times smaller than its APE (Gill et al., 1974), and approximately 90% of the ocean's total KE is contained within the geostrophic eddy field (Ferrari & Wunsch, 2009). This highly energetic dynamical range, termed the oceanic 'mesoscale', spans spatial scales of $\sim 10^4 - 10^5$ meters and temporal scales of weeks to months. Mesoscale flow is comprised of baroclinic and barotropic eddies, current meanders, vortices, waves, and flow filaments that are near quasigeostrophic (QG) balance. Such features shape the ocean circulation by redistributing momentum, transferring energy and information through the water column, dictat-

ing energy dissipation pathways, and influencing physical and biogeochemical tracer mixing. While the satellite era and observational advances have brought about an unprecedented understanding of the large-scale circulation, there remain many unknowns on its vertical structure, and in particular, the influences of mesoscale eddies therein (de La Lama et al., 2016; Stanley et al., 2020). Parameterizing under-resolved eddy influences requires significant efforts in the development of general circulation models (GCMs).

The ocean components of modern state-of-the-art climate models are presently run at resolutions that, at best, only marginally capture mesoscale features within low-latitude regions (Hallberg, 2013). Being in the 'gray zone' of eddy resolution now and over the coming decades presents challenges that older model generations lacked, necessitating scale aware parameterizations that can handle the cross-over from non-eddying to eddy-resolving regimes (Honnert et al., 2020). Under-resolving eddies adversely affects the modelled flow. Effects include mean flows being less energetic due to weakened kinetic energy cascades, suppressed barotropization, erroneous isopycnal structure, and incorrect tracer stirring and mixing representation (Kjellsson & Zanna, 2017). Mesoscale eddy parameterizations have evolved along various avenues over the past decades to correct the modelled flow for such effects. The widely used Gent-McWilliams (GM) parameterization (Gent et al., 1995) mimics APE extraction by eddies through diffusive isopycnal flattening, greatly improving the accuracy of the resolved stratification. More recent efforts have sought to develop prognostic equations for the subgrid eddy KE to inform GM diffusivity (Cessi, 2008; Eden & Greatbatch, 2008), and to reinject KE back into the mean flow in a scale-aware manner (Jansen & Held, 2014; Bachman, 2019; Jansen et al., 2020; Juricke et al., 2020). Alternate approaches to GM have also been developed to represent the effect of Reynolds stresses directly; for example, through potential vorticity mixing (Treguier et al., 1997; Marshall & Adcroft, 2010; Marshall et al., 2012) and through employing a non-Newtonian stress formulation to reinject KE (Zanna et al., 2017; Porta Mana & Zanna, 2014).

Central to all the aforementioned mesoscale eddy parameterization approaches is the energy cycle in oceanic baroclinic turbulence, often described using QG theory. The seminal works of Kraichnan (1967) and Charney (1971) established that 2D and QG flows, respectively, exhibit turbulent behavior characterized by a forward enstrophy cascade to small scales and an inverse KE cascade to large scales. Rhines (1977) and Salmon (1978) developed these arguments in a two-layer QG system, incorporating the idea of barotropization, whereby baroclinic (BC) energy tends to transform into barotropic (BT) energy. A number of works (Held & Larichev, 1996; Thompson & Young, 2007; Gallet & Ferrari, 2021) developed steady-state theories for the two-layer system, all effectively demonstrating that bottom drag can halt the inverse cascade and remove large-scale energy. Fu and Flierl (1980) and K. S. Smith and Vallis (2001) considered multiple baroclinic modes and realistic stratification, showing that baroclinic instability transforms mean available potential energy into high-vertical-mode baroclinic eddy energy at large scales, from whence it moves toward graver modes. Baroclinic energy converges at the length-scale of the Rossby deformation radius, where energy is funneled from the first baroclinic into the barotropic mode, with an efficiency that is reduced by surface-intensified stratification. The inverse cascade occurs predominantly with the fraction of energy in the BT mode. Observations confirm that KE is concentrated in the BT and first BC modes (Wunsch, 1997). However, the majority of observational and modeling studies of vertical structure have been limited by model simplifications, resolution, and availability of vertical data, and therefore may not adequately capture baroclinic vertical structure and barotropic energy fluxes (Chemke & Kaspi, 2016).

The present study aims to guide the improvement of modern mesoscale parameterization schemes that are designed to energize the resolved flow in a scale-aware manner. Such schemes track the energy dissipated by numerical viscosity and GM-type isopycnal flattening and reinject a fraction of that energy back into the large scales (Jansen et al., 2020). The many parameterization and scaling choices embedded in such schemes

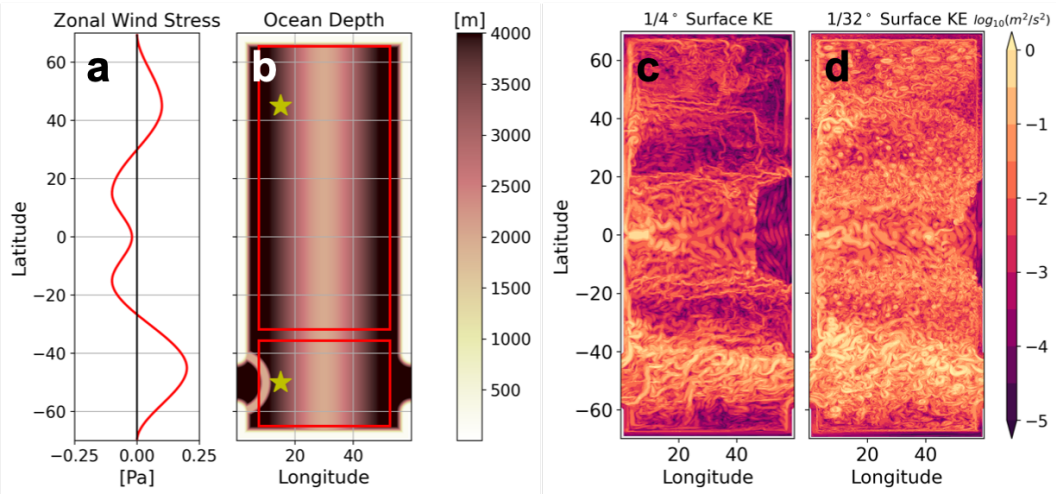

Figure 1. NeverWorld2 configuration: (a) Zonal wind stress in Pascals; (b) ocean depth in meters; 5-day averaged surface kinetic energy density [m^2/s^2] on a logarithmic scale for the (c) 1/4° and (d) 1/32° resolutions. In (b), yellow stars are case study points for which later analysis will be carried out and red boxes are averaging regions for the energy budget calculation.

must be adjusted to produce an accurate parameterized flow, and to guide these choices, one must carefully analyze and understand what determines the distribution of resolved kinetic and potential energy in an eddy-resolving simulation. Here we are particularly interested in understanding the vertical distribution of eddy energy: when backscattered to resolved scales, should it be shunted into the barotropic mode, to mimic the end state of the vertical scale cascade, or is the flow sufficiently resolved to simulate barotropization directly? What fraction of the flow remains baroclinic in eddy-resolving simulations? How does this ratio vary as a function of stratification, latitude, topography, and other resolved-scale features? These questions must be answered in order to to inform the parameterization.

We address these questions using an idealized configuration of the GFDL-MOM6 numerical ocean code (Adcroft et al., 2019), termed 'NeverWorld2', in a hierarchy of grid resolutions (Marques et al., 2022). Section 2 summarizes the NeverWorld2 model setup, presents some key features of its simulated flows, and provides a metric to estimate how well eddies are resolved. In Section 3 we examine the energetics of the flows at different resolutions, decomposed into barotropic and baroclinic modes, and into eddy and mean components, focusing on two dynamically distinct regions of interest. In Section 4, we extrapolate from the two case studies to develop basin-scale ideas about flow vertical structure, eddy dynamics, and the influences of model resolution therein. We end by discussing how our idealized results may be further developed using GCM data and applied to improve existing parameterizations schemes.

2 The NeverWorld2 Model

NeverWorld2 was developed for the investigation of mesoscale eddy dynamics and the development of mesoscale eddy parameterizations. The model is purely adiabatic, with steady zonal wind forcing in an idealized two-hemisphere-plus-channel domain geometry, and shares many aspects with the NeverWorld model of Jansen et al. (2020), hence the name.

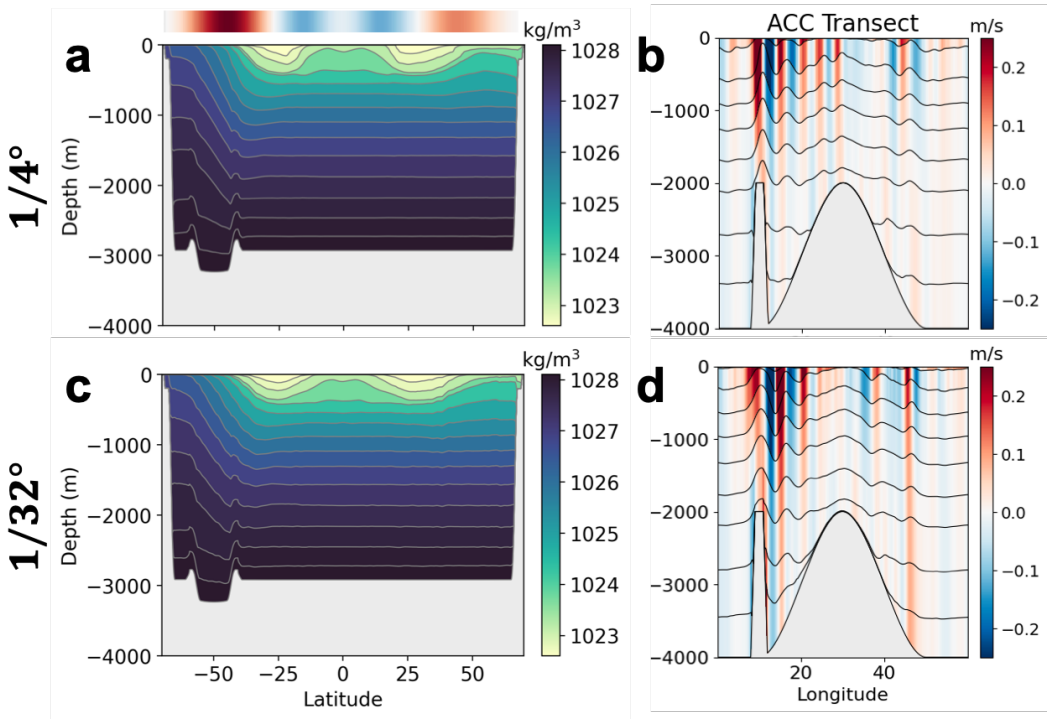

Figure 2. Zonally and 500-day averaged density structure of NeverWorld2 at (a) 1/4° and (b) 1/32° resolutions, with zonal wind stress magnitude above panel (a); the average isopycnal positions are shown as grey contours. 500-day averaged transects of meridional velocity through the ACC at 50°S at (c) 1/4° and (d) 1/32°; isopycnals are shown as black contours.

2.1 Model configuration

We employ the GFDL-MOM6 numerical ocean code (Adcroft et al., 2019) to solve the adiabatic, stacked shallow water equations on a rotating spherical grid, in an idealized one-basin configuration termed 'NeverWorld2' (Marques et al., 2022). The model domain extends from −70°S to 70°N and spans 60° in longitude, with a circumpolar channel near the southern edge of the domain representing an idealized Antarctic Circumpolar Current (ACC) region, with a ridge at the western side representing the Scotia Arc (Figure 1). A 2000 m high gaussian ridge, idealizing the mid-Atlantic ridge, runs the full length of the domain.

The governing momentum and continuity equations satisfied within isopycnal layer k are

$$\partial_t \mathbf{u}_k + (f + \zeta_k)\,\hat{\mathbf{z}} \times \mathbf{u}_k + \nabla(K_k + M_k) = \frac{\boldsymbol{\tau}_{k-1/2} - \boldsymbol{\tau}_{k+1/2}}{\rho_0 h_k} - \nabla \cdot \left[\nu_4 \nabla(\nabla^2 \mathbf{u}_k)\right], \quad (1)$$

$$\partial_t h_k + \nabla \cdot (h_k \mathbf{u}_k) = 0. \quad (2)$$

Here $\mathbf{u}_k = (u_k, v_k)$ is the horizontal velocity, $f = 2\Omega \sin\theta$ is the Coriolis parameter (with $\Omega = 7.2921 \times 10^{-5}$ s^{-1} and latitude θ), h_k is layer thickness, $\zeta_k = \partial_x v_k - \partial_y u_k$ is the relative vorticity, $\hat{\mathbf{z}}$ is the unit vector in the vertical direction, and $\nabla = (\partial_x, \partial_y)$ is horizontal the gradient. The kinetic energy density is

$$K_k = \frac{1}{2}|\mathbf{u}_k|^2 \quad (3)$$

and the Montgomery potential is $M_k = \sum_{l=1}^{k} g'_{l-1/2}\eta_{l-1/2}$, where $g'_{k-1/2} = g(\rho_k - \rho_{k-1})/\rho_0$ is the reduced gravity, ρ_0 is reference density, g is gravitational acceleration, and interface height of the upper layer interface is

$$\eta_{k-1/2} = -D + \sum_{l=k}^{N} h_l. \tag{4}$$

$D(x, y)$ is positive downwards ocean depth, and N is the total number of isopycnal layers (index number increases downward). Gridscale momentum is dissipated by a Smagorinsky biharmonic viscosity (Griffies & Hallberg, 2000) with dynamically-prescribed coefficient ν_4.

Vertical stresses are given by $\boldsymbol{\tau}_{k-1/2} = -A_v\rho_0(\mathbf{u}_{k-1} - \mathbf{u}_k)/h_{k-1/2}$, where $A_v = 1.0\times10^{-4}$ m^2 s^{-1}. The bottom stress is a quadratic bottom drag $\boldsymbol{\tau}_{N+1/2} = -C_d\rho_0|\mathbf{u}_\mathrm{B}|\mathbf{u}_N$, where $\mathbf{u}_\mathrm{B}$ is the flow averaged over the bottom-most 10 m and $C_d = 0.003$. The model is forced only by a surface wind stress, specified by setting the upper stress $\boldsymbol{\tau}_{1/2}$, which is distributed over the top 5 m. The wind stress is zonal, fixed in time, characterized by westerlies in the high latitudes, easterlies in the midlatitudes, and has a maximum peaking at 0.2 Pa in the ACC region (Figure 1a,b). Side boundaries are free-slip, and a free surface is used. There are $N = 15$ isopycnal layers in the vertical and the volume of each layer stays constant as a function of time (due to a lack of buoyancy forcing). Each simulations is initialized from rest, allowed to adjust until it reaches a steady-state, and then run for an additional 500 days, with output saved as 5-day averaged quantities as well as snapshots every 5 days. Additional details of the model can be found in Marques et al. (2022).

2.2 Averaging operators

Throughout the paper, we use various averaging operations, which for a variable $\phi_k(x, y, t)$ are

$$\overline{\phi}^{x}_k = \frac{1}{L}\int_{x_\mathrm{l}}^{x_\mathrm{r}} \phi_k \,\mathrm{d}x \qquad \text{— zonal average} \tag{5}$$

$$\overline{\phi}^{t}_k = \frac{1}{T}\int_{0}^{T} \phi_k \,\mathrm{d}t \qquad \text{— time average} \tag{6}$$

$$\overline{\phi}^{z} = \frac{1}{D}\sum_{k=1}^{N} h_k\phi_k \qquad \text{— depth average} \tag{7}$$

$$\{\phi_k\} = \iint_\mathrm{domain} G(\mathbf{x} - \mathbf{x}')\phi_k(\mathbf{x}')\,\mathrm{d}\mathbf{x}' \quad \text{— spatial filter.} \tag{8}$$

Here $L = L(y) = x_r(y) - x_l(y)$ is the y-dependent domain width, $t = 0$ denotes the start of the $T = 500$ day analysis period, $\mathbf{x} = (x, y)$, and $G(\mathbf{x})$ is the filtering kernel definied in Grooms et al. (2021). A Python package for this filter is provided by Loose et al. (2022).

2.3 Lateral resolution hierarchy

The central control variable considered in this work is the model's lateral grid resolution, consisting of four baseline cases: 1/4°, 1/8°, 1/16°, and 1/32°. To get a sense of the effect of resolution on the simulated flows, Figure 1c,d shows the surface KE at 1/4° and 1/32°, respectively. The flow is clearly much richer at the highest resolution.

One can also begin to appreciate the differences in density structure as a function of resolution (Figure 2a,c). At 1/4° the temporally and zonally averaged isopycnals in the ACC region as well as the midlatitude gyres (around 30°N and 30°S) have relatively steep slopes. In the higher resolution case, mesoscale eddies are better resolved and act

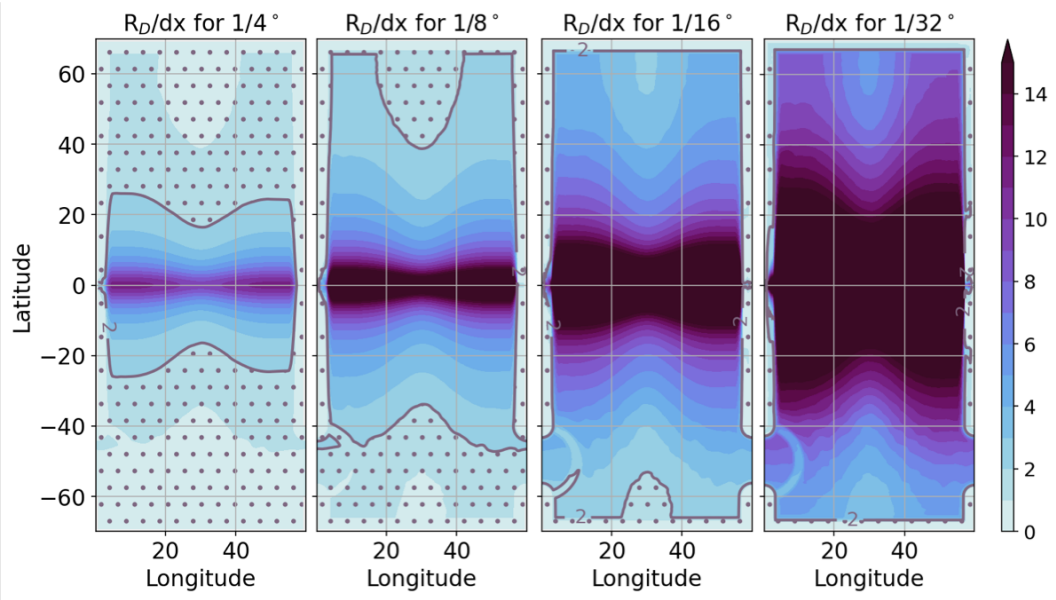

Figure 3. Comparison of the degree to which the first baroclinic Rossby deformation radius is resolved for the various resolutions of NeverWorld2 considered in this study. The $R_\mathrm{D}/\Delta x$ metric (where Δx is zonal grid spacing) is plotted. The purple-grey isoline indicates where $R_\mathrm{D}/\Delta x = 2$, which we consider a rough cutoff between eddy resolving ($R_\mathrm{D}/\Delta x > 2$) and non-eddying ($R_\mathrm{D}/\Delta x < 2$) shown with dots.

to restratify the flow through isopycnal flattening. The midlatitude gyres appear more surface intensified, and the near-surface stratification throughout the domain is higher. A prominent dynamical feature is evident in the time-averaged meridional velocities taken in a zonal transect through the ACC: the presence of barotropic standing meanders (Figure 2b,d). Although some surface intensification is evident, the velocities associated with the meanders remain significant through the entire water column.

How well-resolved are eddies in each case? To answer this, we must define a metric. This is complicated by the nonlinear interactions which are a hallmark of oceanic flows. Resolving the dominant eddy lengthscale alone may not be sufficient in capturing many of the relevant dynamics that shape eddy properties. A better measure is how well the eddy forcing by baroclinic instability is resolved. According to the classic model of linear baroclinic instability (Eady, 1949), the Rossby radius of deformation R_D is close to the most baroclinically unstable lengthscale. The diagnostic $R_\mathrm{D}/\Delta x$, where Δx is the zonal grid spacing, is computed online in MOM6 by solving a vertical mode problem and shown in Figure 3 for each resolution. Note that Δx varies with latitude and is largest near the equator (Δy remains constant), and that $R_\mathrm{D}/\Delta x$ increases mostly linearly with increasing resolution due to the decrease in Δx. A more accurate analysis using regional linear QG instability calculations to compute the scales of the fastest growing modes is given in Appendix A.

Based on the Nyquist theorem, we assume that to resolve eddies, at least two grid boxes must fall within the deformation radius, i.e. $R_\mathrm{D}/\Delta x \geq 2$. The isoline where this is minimally satisfied is plotted in purple-grey, and dotted regions are non-eddy resolving by this metric. The majority of the domain in the 1/16° and 1/32° simulations satisfy this criterion. At the 1/4° case, only the equatorial region (where eddy-driven dynamics are less applicable due to the decreased Coriolis parameter) does so. Thus, we

consider the 1/4° case to be broadly non-eddy-resolving and the 1/32° case to be well-resolved. As validation for the use of NeverWorld2 as an idealized analog to a more realistic GCM, we also examined $R_D/\Delta x$ for the 1/4° GFDL OM4 (Adcroft et al., 2019). Broadly, there is agreement with the 1/4° NeverWorld2 simulation, although OM4 has slightly poorer eddy resolution (not shown). The agreement indicates that NeverWorld2 is representative of how an analogous resolution GCM would resolve mesoscale eddies.

3 Influences of resolution on flow energetics

Here we assess energetic properties and flow partitioning between BT, BC, mean, and eddying components across the various NeverWorld2 resolutions. We will consider how changes observed in the flow as resolution is increased are shaped both by changes in the extent to which mesoscale eddies are captured and the underlying dynamical regime.

3.1 Kinetic and potential energy as functions of latitude and resolution

Figure 4 illustrates the zonal-, time- and depth-averaged KE density $\overline{K}^{x,z,t}$ and APE density $\overline{P}^{x,t}$ as functions of resolution and latitude, where K is defined in (3) and the APE is

$$P = \frac{1}{2D} \sum_{k=1}^{N} g'_{k-\frac{1}{2}} \left(\eta_{k-\frac{1}{2}} - \eta^{\text{ref}}_{k-\frac{1}{2}} \right)^2 , \tag{9}$$

where $\eta^{\text{ref}}_{k-\frac{1}{2}}$ is the resting reference state, adjusted to follow topography when outcropping[1]. Note that unlike K, the APE P is defined as a column-integrated quantity.

As expected, the KE decreases by more than half between the high-resolution 1/16° and 1/32° cases and the low-resolution 1/4° case. The APE has the opposite trend, decreasing as the resolution is increased. Again, this is expected as mesoscale eddies feed off of the large-scale APE of the flow and when eddies are under-resolved there is less of an APE sink. The APE is two orders of magnitude larger than the KE, and both KE and APE peak in the south, where isopycnals outcrop near the ACC.

Figure 4c shows the ratio of eddy available potential energy (EAPE) to eddy kinetic energy (EKE). Defining 'eddy' as a deviation from the time-mean and denoting this with a prime, the eddy velocity and EKE are

$$\mathbf{u}'_k = \mathbf{u}_k - \overline{\mathbf{u}_k}^t. \tag{10}$$

and

$$\text{EKE} = \overline{\frac{|\mathbf{u}'_k|^2}{2}}^z , \tag{11}$$

respectively. Likewise, EAPE is defined as in (9), but using $\eta'_k = \eta_k - \overline{\eta_k}^t$ instead of η_k. Using these definitions, and (5)–(7), Figure 4c shows $\overline{\text{EAPE}}^{x,t}/\overline{\text{EKE}}^{x,z,t}$. In the higher resolution cases, there is equipartitioning between eddy APE and KE, with their ratio near 1 throughout the domain. APE fluctuations presumably provide the energy source for the KE fluctuations. However, at 1/4°, there is significantly more EAPE than EKE and the ratio deviates substantially from the 'truth'. Such high values indicate that the transfer of APE into KE is not being resolved. The pattern of this error is noteworthy — the largest discrepancy is in the northernmost part of the domain, where EAPE/EKE $\sim O(10)$. There is greater discrepancy between the higher-resolution cases in the northern region as well. Meanwhile, in the ACC where we see the largest discrepancies rel-

[1] Note that APE defined in this manner constitutes a part of the net PE, corresponding to the displacement of isopycnals from a rest state using a spatially varying reference level unique to each isopycnal and corresponding to a motionless state. PE on its own refers to the position of isopycnals relative to a constant, global reference level.

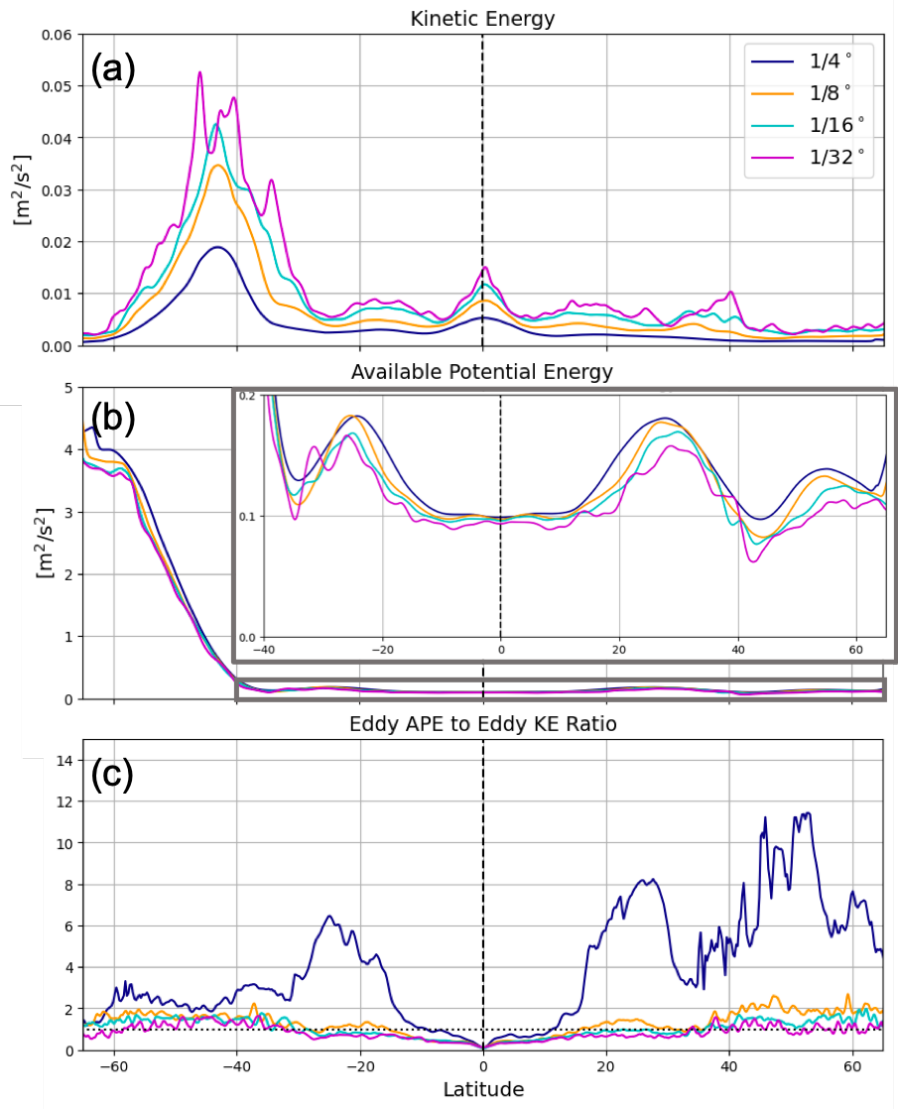

Figure 4. Vertically integrated, zonally and 500-day averaged plots of (a) KE, (b) APE, and (c) the ratio of EAPE to EKE (specifically, $\overline{\mathrm{EAPE}}^{x,t}/\overline{\mathrm{EKE}}^{x,z,t}$) as a function of resolution. In (b), a zoomed-in view is shown of the region outlined in grey outside the ACC where APE is significantly smaller. Energies are plotted as energy densities with units of [$\mathrm{m}^2\ \mathrm{s}^{-2}$]. In (c), we employ the temporal definition of eddy.

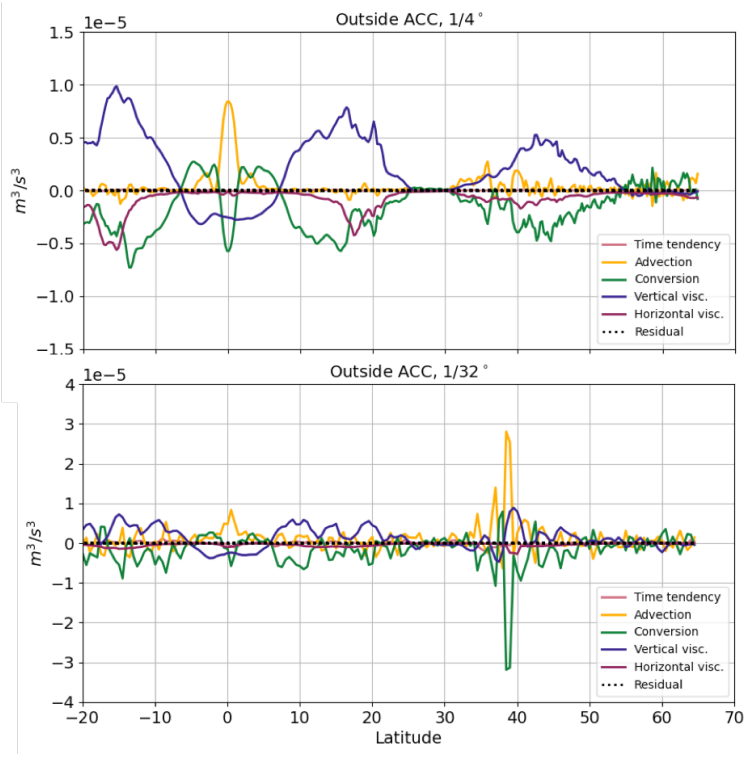

Figure 5. Vertically integrated, zonally and 500-day averaged plots of KE budget terms for the 1/4° and 1/32° cases for the NeverWorld2 domain outside of the ACC (see red boxes in Figure 1b).

ative to the high resolution case in mean KE and APE, the eddy properties only deviate slightly for the various resolutions. The northern hemisphere's eddy dynamics appear significantly more sensitive to increasing resolution. This is partially explainable by the smaller-scale (thus less resolved) unstable modes found in the northern part of the domain compared to the ACC (Figure A2). The difference in dynamical regime may be another contributing factor, discussed in later sections.

3.2 Kinetic energy budget

Here we investigate the tendency, flux, and dissipation terms that determine the local kinetic energy. To wit, the kinetic energy budget for layer k is

$$\underbrace{\partial_t \left(h_k K_k\right)}_{\text{tendency}} + \underbrace{\nabla \cdot \left(h_k \mathbf{u}_k K_k\right)}_{\text{advection}} \tag{12}$$

$$= \underbrace{- h_k \mathbf{u}_k \cdot \sum_{l=1}^{k} g'_{l-\frac{1}{2}} \nabla \eta_{l-\frac{1}{2}}}_{\text{conversion}} + \underbrace{h_k \mathbf{u}_k \cdot \frac{\boldsymbol{\tau}_{k-1/2} - \boldsymbol{\tau}_{k+1/2}}{\rho_0 h_k}}_{\text{vertical visc.}} - \underbrace{h_k \mathbf{u}_k \cdot \nabla \cdot \left[\nu_4 \nabla (\nabla^2 \mathbf{u}_k)\right]}_{\text{horizontal visc.}}, \tag{13}$$

The labeled terms are computed, vertically integrated, 500-day and zonally averaged, and plotted for the 1/4° and 1/32° cases outside the ACC region in Figure 5, and in the ACC region in Figure 6. In all cases, the time tendency is near zero, indicating steady state. The vertical viscous term includes removal of energy through vertical dissipation and bottom friction, as well as the input of energy by surface wind stress. Outside of the

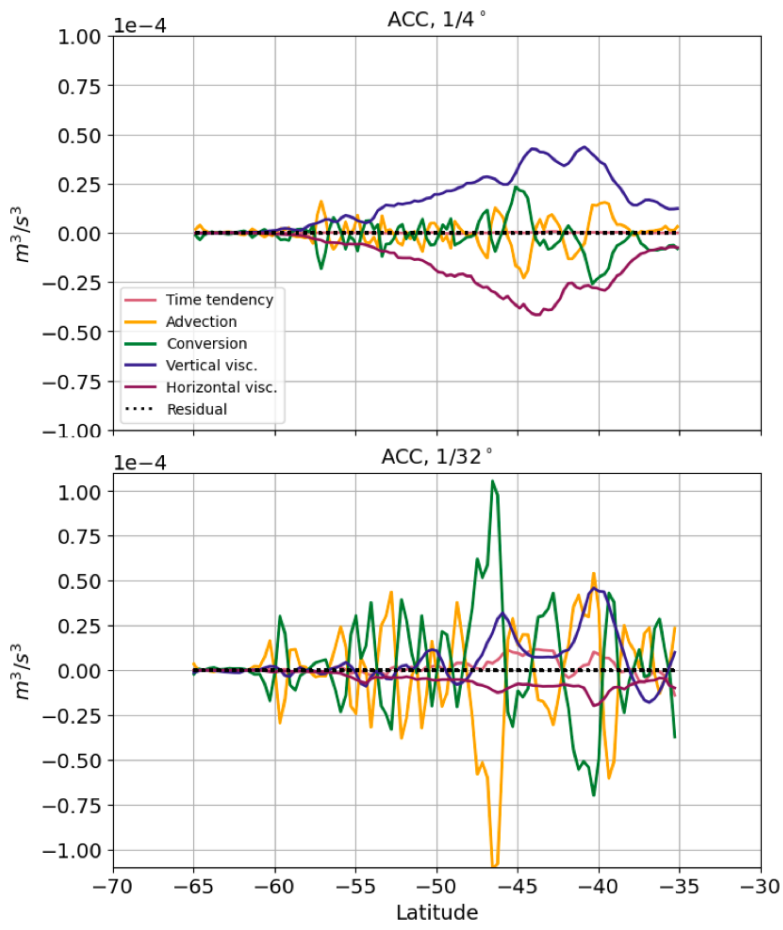

Figure 6. Same as Figure 5, but for the ACC region.

ACC (Figure 5) the KE budgets are similar different between the two model resolutions. Wind stress KE input is removed by conversion to PE through geostrophic adjustment and by horizontal viscous dissipation in both cases. The main difference between the two resolutions is that advection is larger in magnitude in the higher-resolution case and in some regions balances the conversion term. This is indicative of a more vigorous and non-local eddy field. The other, more subtle difference is that the net vertical viscous term is smaller in the 1/32° case. Since the wind stress in the two cases is the same, this means that the negative vertical dissipation and bottom drag are enhanced in the higher resolution case. Enhanced dissipation through bottom drag at higher resolution is consistent with a fully-resolved vertical and horizontal inverse energy cascade, resulting in large-scale, nearly barotropic eddy energy that is removed primarily by bottom friction.

A feature that stands out at both resolutions is the difference between the ACC and the rest of the domain. In the ACC, the budget terms are nearly an order of magnitude higher. At 1/4° in the ACC there is an approximate balance between the vertical viscous term creating a net positive input of energy and the horizontal viscous dissipation. There are strong, roughly balanced fluctuations in the conversion of PE to KE and advection of KE — indicative of eddy activity in this region at both resolutions. The conversion and advection terms are particularly large and noisy in the 1/32° case. Here eddies facilitate more efficient transfers between PE and KE and increase advection of

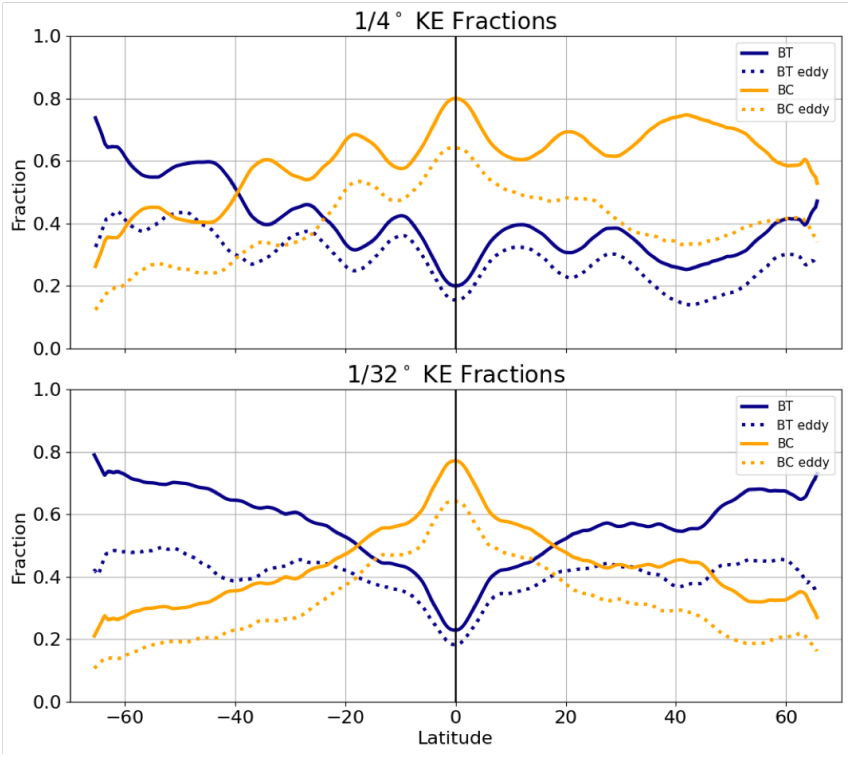

Figure 7. Vertically integrated, zonally and 500-day averaged plots of the fractions of KE in the BT, BC, and eddy parts of the flow, computed based on 15 and (16). Note that the BT and BC mean flow components are not plotted but can be inferred (mean BT and eddy BT sum to total BT, and likewise for BC). The top and bottom plots are for the 1/4° and 1/32° cases, respectively.

KE. More dissipation is again occurring through bottom drag, evidenced by the smaller magnitude of the net vertical viscous term and diminished horizontal dissipation.

Thus, in both regions the primary difference between the low- and high-resolution cases is the larger fluctuation in PE-to-KE conversion and KE advection, as well as the increased role of bottom drag in dissipation. All regions undergo a shift from horizontal viscosity-dominated dissipation at lower resolution to dissipation through bottom drag at higher resolution. The latter serves as indirect evidence of an increasingly barotropic flow that feels the bottom as the resolution increases, indicating more efficient vertical transfer of energy by eddy activity and a more physically-realistic dissipation pathway consistent with the QG energy cycle.

3.3 Vertical and eddy-mean energy partitioning

We next consider the partitioning between barotropic (BT) and baroclinic (BC) mean and eddy kinetic energy, averaged zonally and considered as functions of resolution. Defining BT and BC velocities as

$$\mathbf{u}_{\mathrm{BT}} = \overline{\mathbf{u}_k}^z \quad \text{and} \quad \mathbf{u}_{\mathrm{BC},k} = \mathbf{u}_k - \overline{\mathbf{u}_k}^z, \tag{14}$$

we define the total BT and BC kinetic energies as

$$K_{\mathrm{BT}} = \frac{1}{2}\mathbf{u}_{\mathrm{BT}}^2 \quad \text{and} \quad K_{\mathrm{BC}} = \frac{1}{2}\overline{\mathbf{u}_{\mathrm{BC},k}^2}^z. \tag{15}$$

and the modal eddy kinetic energies as

$$K_{\mathrm{BT,eddy}} = \frac{1}{2}(\mathbf{u}'_{\mathrm{BT}})^2 \quad \text{and} \quad K_{\mathrm{BC,eddy}} = \frac{1}{2}\overline{(\mathbf{u}'_{\mathrm{BC},k})^2}^z. \tag{16}$$

Using these definitions, Figure 7 shows for the lowest and highest resolution simulations the total and eddy fractions of kinetic energy in the barotropic and baroclinic modes, averaged zonally, i.e.

$$\text{BT fraction} = \overline{K_{\mathrm{BT}}/\overline{K}^z}^{x,t} \tag{17}$$

$$\text{BC fraction} = \overline{K_{\mathrm{BC}}/\overline{K}^z}^{x,t} \tag{18}$$

$$\text{eddy BT fraction} = \overline{K_{\mathrm{BT,eddy}}/\overline{K}^z}^{x,t} \tag{19}$$

$$\text{eddy BC fraction} = \overline{K_{\mathrm{BC,eddy}}/\overline{K}^z}^{x,t}. \tag{20}$$

The ratios differ substantially between the low and high resolution cases. At $1/4°$, outside of the ACC most of the KE is in the BC part of the flow. At $1/32°$, aside from the equatorial region the BT part of the flow is dominant. Significant barotropization occurs as we move from low to high resolution — consistent with prior studies of realistic GCM hierarchies (Kjellsson & Zanna, 2017; Griffies et al., 2015). The only exception is the ACC region, where even at $1/4°$ the flow is already mostly BT and remains so as resolution is increased. In the mean/eddy partitioning, the dominant trend is a substantial increase in the eddy component at high resolution. The mean KE also has less latitudinal variability, particularly in the BC mean part. For example, in the $1/4°$ case around $45°N$ there is a peak in eddy and mean BC KE, indicating trapping of energy in the BC modes and unresolved eddy dynamics; this feature disappears in the $1/32°$ case. The mean KE fraction in both the BT and BC modes decreases to about 10-20% of the total KE at high resolutions. This fraction is consistent with the findings of Ferrari and Wunsch (2009) that 90% of the ocean KE is in the geostrophic eddy field. Thus, increasing resolution has the effect of increasing KE, with the greatest fraction ending up in the BT eddy component. The flow partitioning is least dependent on resolution when background flow is barotropic, and most sensitive when mean flow is weak and baroclinic, such as the northern hemisphere around $30 - 60°N$.

Figure 9 is analogous to Figure 7, but with 'eddy' now based on a deviation from a *spatial average*, which requires some explanation. We employ a package developed for spatial filtering of geophysical data (Grooms et al., 2021; Loose et al., 2022) to isolate the mesoscale eddy field. To account for inverse cascade-driven eddy growth, the filter scale is taken as $5\overline{R_{\mathrm{D}}}^x$, but limited to 500 km in the equatorial region (Figure 8). Following the spatial filtering, defined in (8), we time average to remove the stationary part of the flow, thus for Figure 9, 'eddies' are defined as

$$\mathbf{u}'_k = (\mathbf{u}_k - \{\mathbf{u}_k\}) - \overline{(\mathbf{u}_k - \{\mathbf{u}_k\})}^t. \tag{21}$$

Mean and eddy KE fields are then computed from the decomposed velocities as in (16). The advantage of this approach is its scale-aware dependence on the local deformation radius. Both R_{D} and the eddy energy-containing scales have a strong latitudinal dependence, which is accounted for through this filtering approach. Further, this eddy definition includes only the small-scale fluctuating flow, unlike the prior definition where all fluctuating flow regardless of scale was considered eddying.

With spatial filtering included in the definition of eddy, kinetic energy at high resolution is no longer dominated by the eddying flow. Instead, the BT mean flow dominates outside of the equatorial region. There is equipartitioning between BC and BT eddy components outside of the equator. This is not true in the low-resolution case, where the BC eddy component is roughly twice as large as the BT eddy component (outside the ACC), reaffirming the lack of resolved energy fluxes from the BC modes into the BT mode,

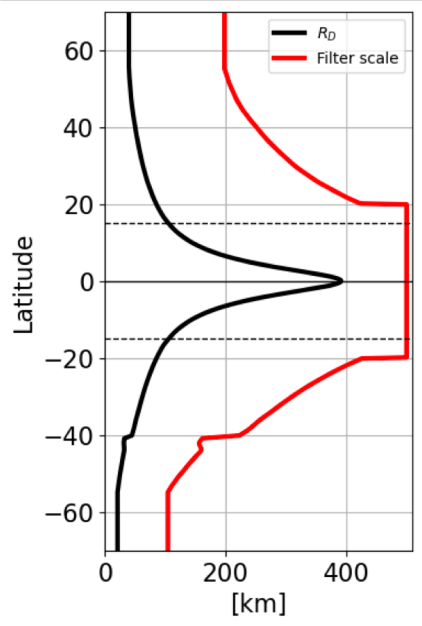

Figure 8. Filter scale for the spatial filtering as a function of latitude (red) and the zonally averaged first baroclinic Rossby deformation radius, R_D (black).

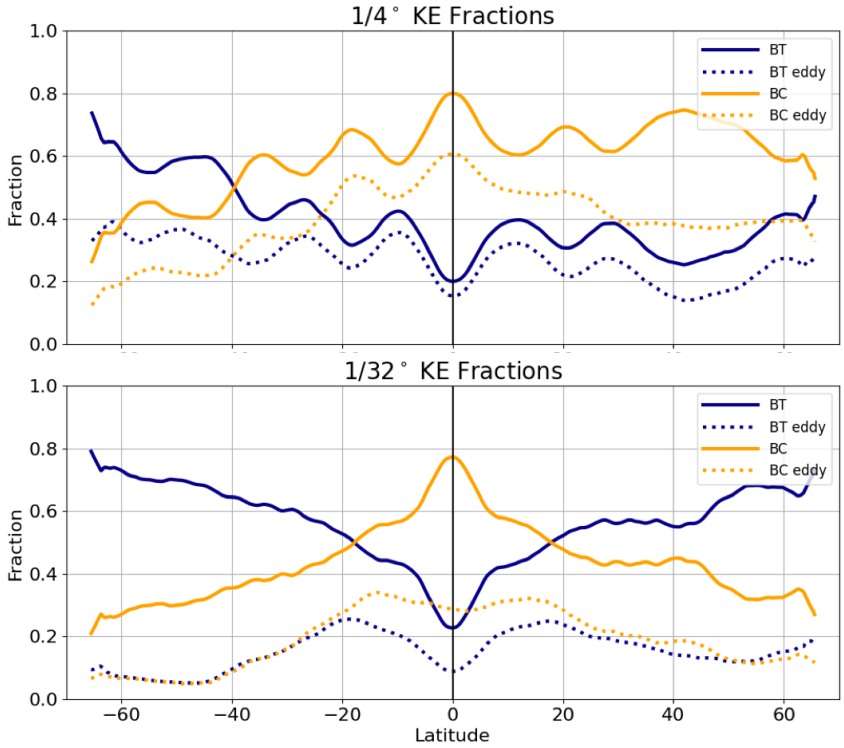

Figure 9. As in Figure 7, but with eddy components defined based on combined temporal and spatial filtering. The total BT and BC KE are repeated for reference.

and lack of an inverse cascade in the BT mode. In the ACC the dynamics change less with resolution (as in Figure 7) and are mostly dominated by the mean flow. This filtering approach considers features such as standing meanders to be part of the mean flow, and as shown in Figure 2 the ACC is characterized by strong BT standing meanders. Such features are dominating the energetic balance in the ACC and are only mildly sensitive to increasing resolution. Thus, the spatial filtering approach is successful in capturing the effect of mesoscale baroclinic eddies and their energetic transfers in the high-resolution case. However, both approaches yield similar insights into the deficiencies in vertical structure representation at low resolution. The distinction between mean and eddying flow becomes less important as the eddy-driven inverse cascade progresses, moving energy to larger scales, barotropizing the flow, and leading to bottom-enhanced dissipation. Both approaches can be used to diagnose ill-represented dynamics, though the mesoscale eddy character is better isolated in the spatially filtered, scale aware definition.

4 Vertical Structure of Eddy Energy and Influences on Mean Flow

Through the previous analysis, two distinct regimes stand out in how their vertical structure changes as a function of resolution. One is the ACC, where at coarse resolution the deformation radius is unresolved yet the vertical structure and mean/eddy partitioning does not change significantly with increasing resolution. The other is the northern hemisphere outside the equatorial region, where the most unstable scales are significantly smaller than the deformation radius. There, all the metrics we consider for vertical structure are indicating that the transfer of BC to BT KE and the inverse cascade in the BT mode are unresolved at coarse resolution. As resolution increases, the BT KE fraction substantially increases. We will now isolate two points within these regions to obtain a more detailed look at the vertical structure of density, momentum, and energy. The first point is in the northwest (NW) of the domain, the second point is in the western ACC — see Figure 1 for reference. We will then consolidate results from the two case studies and previously considered zonal properties to yield a basin-wide view of mesoscale eddy influences on flow vertical structure.

4.1 Two case studies

Figure 10 shows the time series of BC and BT KE at the NW location. At 1/4° a dominant portion of the KE is BC, whereas at 1/32° a larger portion is BT. In both cases, there is significant temporal variability in the KE field. The figure also shows vertical isopycnal fluctuations as a function of depth; the standard deviation and maximum displacements are computed at each average vertical isopycnal position. Strong contrast is evident between the vertical structure of isopycnal fluctuations between the two resolutions. The fluctuations are surface intensified at 1/4°, and nearly an order magnitude larger and spanning the entire water column at 1/32°. This supports the previous evidence for strong barotropization with resolution observed outside of the ACC and equatorial regions. Figure 11 shows the same comparison for the ACC. Here the dynamics are already significantly BT at the 1/4° case. Comparable BT and BC KE is observed in the time series, and the isopycnals have large and somewhat uniform with depth fluctuations throughout the water column. Increasing the resolution does not appear to change the vertical structure of the flow appreciably.

In order to consider the vertical structure and BT/BC KE and APE partitioning in greater detail we compute the vertical KE and APE energy spectra at two locations investigated in this subsection. The spectra are created by first computing the local vertical modes, projecting onto them the velocities and isopycnal dispacements, then computing the spectra. See Appendix B for details. The resulting spectra are shown as spectra in Figure 12.

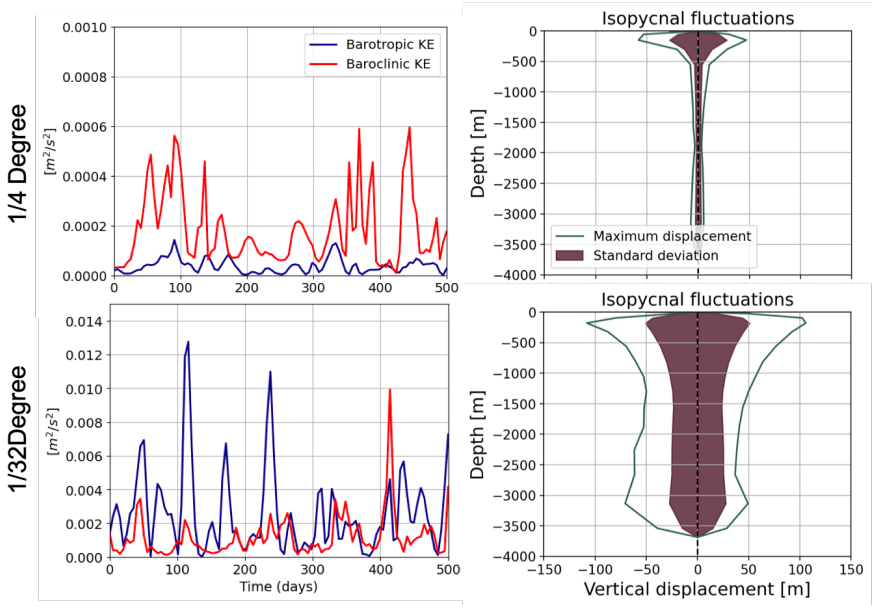

Figure 10. Northwestern region of NeverWorld2 (see star in Figure 1): timeseries of BT and BC KE and vertical isopycnal fluctuations as a function of depth for the 1/4° (top) and 1/32° (bottom) cases. The purple envelope shows the standard deviation of isopycnal fluctuations, and the green line shows the maximum vertical displacement.

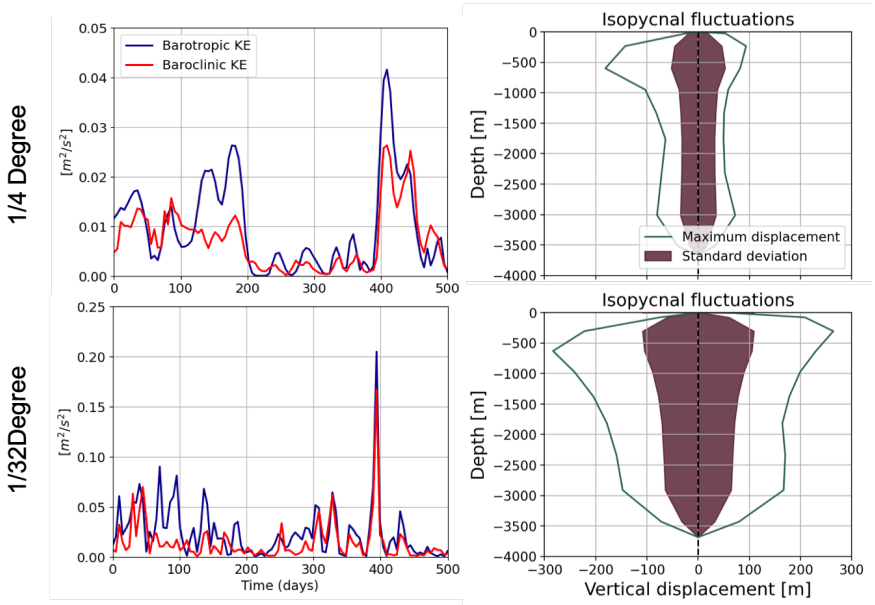

Figure 11. Same as Figure 10 but for the ACC region; note the different axes scales.

The top panel of Figure 12 elucidates the inaccuracies in PE and KE structure in the 1/4° case relative to the high resolution case. The BT mode energy is shown by the arrow, and each BC mode is denoted by a point (higher mode numbers correspond to smaller vertical scales). First, it is apparent that the net KE is lower at 1/4° than in the 1/32° resolution (consistent with Figure 4). More critically, energy in the BT mode at

1/4° is significantly lower than in the BC modes and that of the higher resolution. The first BC mode is also much less energetic, in large part due to the buildup of energy in the higher modes. There is a peak at the second and third BC modes, indicating energy is trapped and not cascaded into graver modes or barotropized. The higher resolution cases have comparable slopes to the -3 value predicted by Charney (1971) for the vertical energy spectrum in a region far from boundaries. The same problem of overly-shallow spectra at small wavenumbers exists both in the PE and KE spectra at coarse resolution.

The bottom panel of Figure 12 shows the same spectra for the ACC region. Here, all resolutions have a similar vertical structure and well-energized BT modes. The 1/4° case is still less energetic, particularly in the BT mode, than the higher resolution cases. Nonetheless, the overall spectral shape is similar among all resolutions. These results reaffirm those of the previous section. Traditional baroclinic-eddy driven dynamics are dominating in the northern part of the domain — when these eddies are not resolved there is significant energy trapping in high baroclinic modes and the vertical structure of the flow fails to become barotropic. On the contrary, the ACC dynamics are driven by BT eddies and standing meanders that are already capturing the BT flow signature at 1/4° resolution.

4.2 Basin-wide view

We now synthesize the above analysis by considering the basin-wide behavior of barotropization and a metric that may explain how the BT/BC partitioning is set. Figure 13 shows a domain-wide comparison of BT KE fractions at 1/4° and 1/32° as well as the change in the BT KE fraction between the two resolutions. Interestingly, the change in BT KE fraction as a function of resolution is dictated partly by the initial energy content in the BT mode. In the south, where the BT KE fraction is high, the change in BT KE fraction is low, and in the north (where at 1/4° BT KE is minimal) the change is maximal. We next consider what may govern the BT KE fraction as a function of latitude, allowing us to anticipate discrepancies in the vertical structure at coarse resolution.

A possible explanation for the BT KE fraction and its latitudinal dependence is based on considering the extent of the inverse cascade region (Larichev & Held, 1995). As discussed in the introduction, the inverse cascade in the BT mode begins roughly at the deformation radius R_{D}. The energy is moved upscale toward the energy containing scale R_{E}, at which KE exhibits a spectral peak. The lengthscale R_{E} may be set by domain size, topographic effects, or the Rhines scale. Our hypothesis is that the larger the scale separation between R_{D} and R_{E}, the larger the range over which barotropization will occur and the greater the final BT KE fraction will be. According to Larichev and Held (1995) the ratio $(R_{\mathrm{E}}/R_{\mathrm{D}})^2$ scales roughly as the ratio of BT to BC eddy KE (although in a more idealized system than the one considered here).

In Figure 14 we test the above hypothesis. The top subplot shows two approaches for computing the energy containing scale R_{E}. In the first approach, eddy KE spectra (using meridional velocities) are computed at each latitude and the spectral peak is obtained. When computing spectra, velocities are taken along a constant latitude and interpolated onto a Cartesian grid, with coordinates defined in km rather than degrees. Detrending and a Hann window are applied. The spectral peaks are found at each time index and results are averaged over 100 days. This approach proves somewhat problematic as many regions, in spite of detrending and smoothing, retain peak energy values close to the largest resolvable scales. This issue is heightened in the high latitude regions, where the size of the domain becomes substantially smaller and the spectra have coarser resolution at the low wavenumbers. A second approach discussed in Tulloch et al. (2011) is to compute the centroid wavenumber k_C of the eddy KE spectrum.

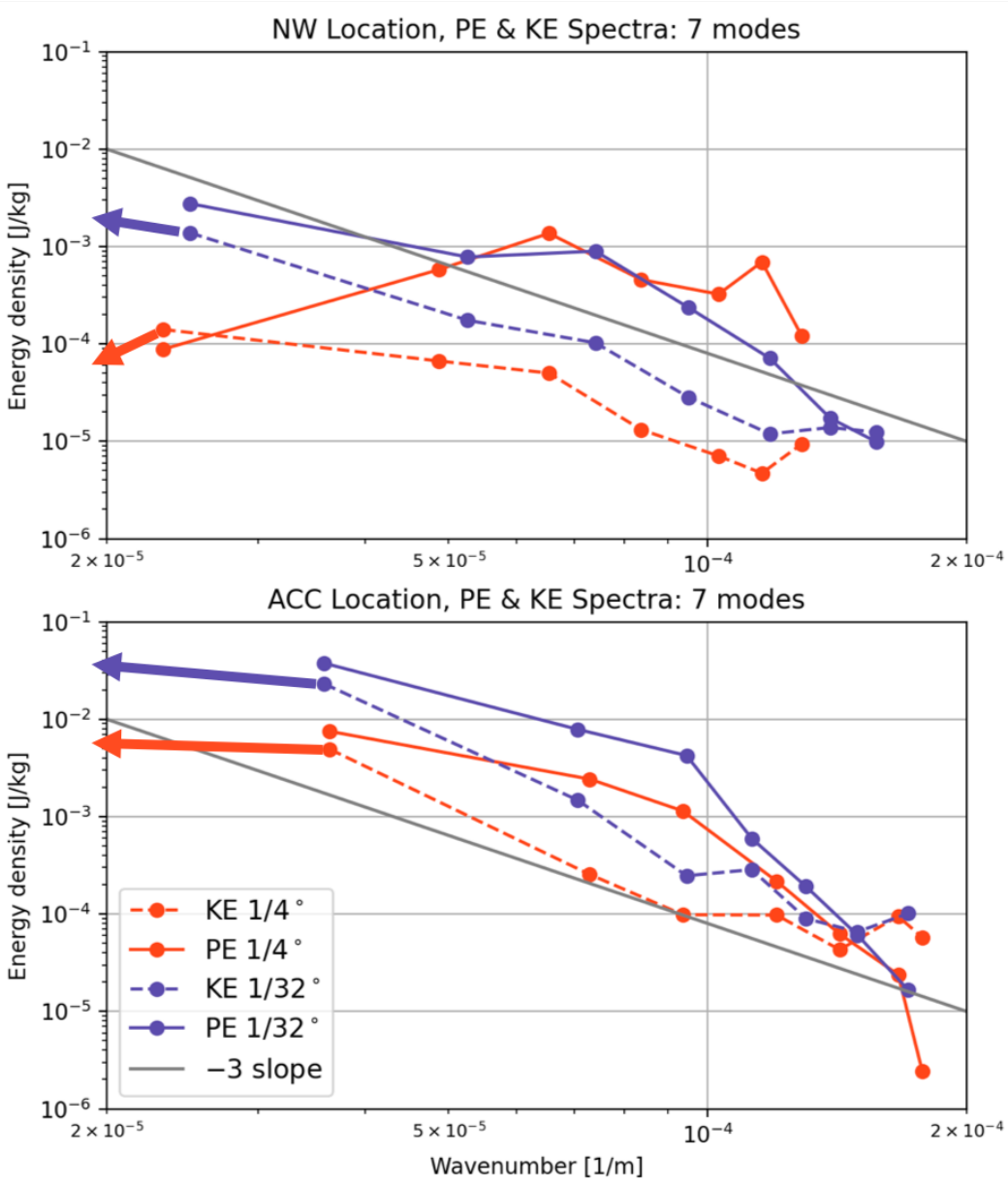

Figure 12. Upper panel: Northwestern region of NeverWorld2 (see star in Figure 1); Lower panel: ACC region. Shown are the PE (solid lines) and KE (dashed lines) spectra as a function of vertical wavenumber for 1/4° and 1/32° resolutions. Each point corresponds to a vertical mode, with the arrows on the y-axis indicating the energy density of the BT (zeroth) mode. The grey line shows the -3 slope predicted by Charney (1971) for the vertical energy spectrum in a region far from boundaries, obeying horizontally homogeneous QG dynamics.

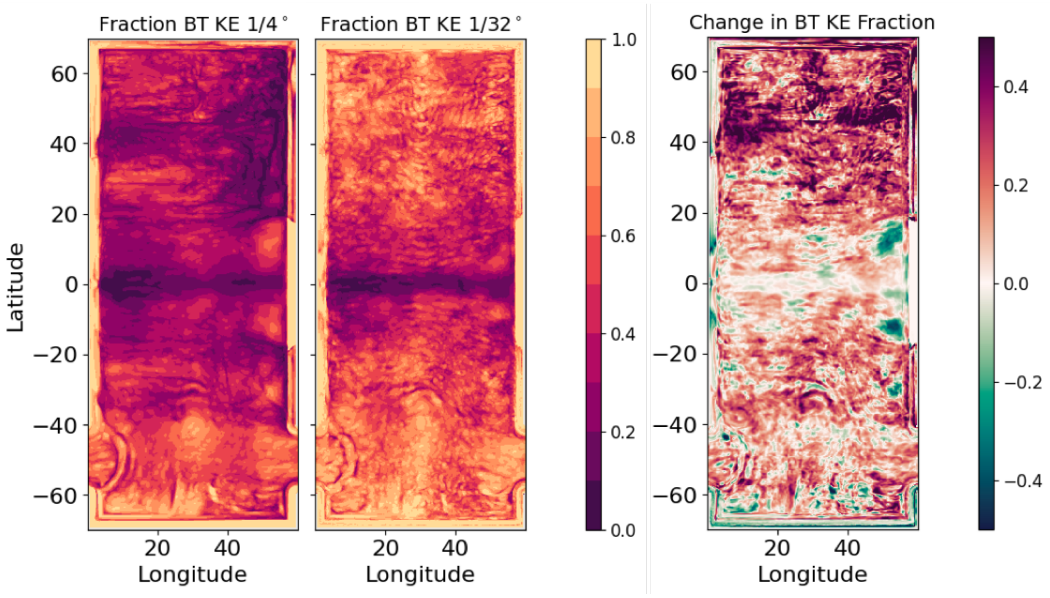

Figure 13. Shown are domain-wide BT KE fractions for the 1/4° and 1/32° cases. The amount of barotropization from low to high resolution is shown in the rightmost panel.

In Figure 14 we see that the centroid approach generally gives smaller values with less spread for R_{E}, while the spectral approach yields larger scales with more spread due to the coarse resolution at small wavenumbers. Nonetheless, both of these both of these approaches result in $R_{\mathrm{E}}/R_{\mathrm{D}}$ highly correlated with BT/BC eddy KE ratio. The spectral peak approach in particular has $R_{\mathrm{E}}/R_{\mathrm{D}}$ nearly following the BT/BC eddy KE ratio throughout all latitudes. Thus, as scale separation between R_{E} and R_{D} increases there is indeed more of an inverse cascade giving rise to more BT flow (consistent with Larichev and Held (1995)). This may be leveraged to guide how the vertical structure of a coarse resolution model should be corrected in a mesoscale eddy parameterization scheme — for instance, energy may be reinjected to the large-scale barotropic component of the flow in a scale-aware manner.

5 Summary & Discussion

We have systematically considered the effects of mesoscale eddies on energetic properties and flow vertical structure in the idealized model hierarchy NeverWorld2 (Marques et al., 2022). We began by characterizing the extent to which mesoscale eddies are resolved at 1/4°, 1/8°, 1/16°, and 1/32° resolutions using two criteria for lengthscale — the Rossby deformation radius R_{D} and the local most unstable wavelength R_{MAX} (generally several times smaller than R_{D}). We find that by these metrics the 1/4° and 1/8° cases are marginally eddy-resolving in low latitudes, while the 1/16° and 1/32° cases are mostly eddy-resolving. We examined the zonally averaged KE and APE structure of NeverWorld2 and found that as resolution degrades there is significantly less KE and more APE. The ratio of eddy APE to eddy KE converges among the higher-resolution cases towards value of 1.0 (indicating equipartitioning), but is significantly higher at 1/4°. A profound shift in the vertical structure of KE occurs between non-eddy resolving and eddy resolving cases, similar to that observed by Kjellsson and Zanna (2017). At low resolution, KE is mostly baroclinic and the flow fails to barotropize; this is accentuated in regions with weak and baroclinic background flow and regions where R_{MAX} is on smaller scales. As the vertical energy fluxes associated with mesoscale eddies are increasingly

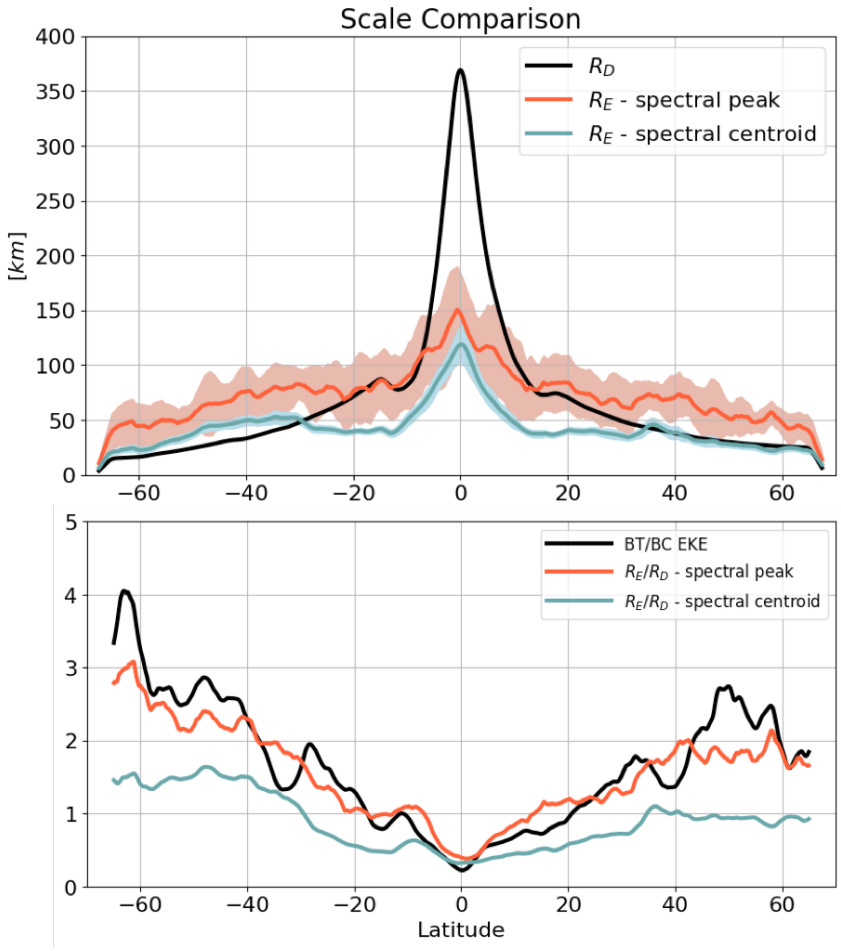

Figure 14. The top panel shows the zonally averaged values of R_{E} computed using spectral peaks and a centroid approach for the 1/32° case. The lower panel shows the ratios of energy containing scale to deformation radius computed using the two approaches as well as the BT to BC eddy KE ratio. Shading shows the standard deviation.

resolved, the issue of BC energy trapping is mediated and the flow is able to barotropize. An interesting exception occurs in the ACC, where the background flow is barotropic at low resolution. Here, the vertical structure and flow partitioning is much less sensitive to the extent to which R_{D} or R_{MAX} are captured.

The KE budget shows a similar response to eddy resolution and dynamical regime. The ACC is least sensitive to resolution and even at coarse resolutions exhibits significant dissipation through bottom drag. Elsewhere, there is a trend of horizontal viscous dissipation diminishing and dissipation through bottom drag becoming dominant with increasing resolution. This is consistent with the observed pattern of barotropization and the QG energy cycle (Larichev & Held, 1995); as the BT KE fraction becomes more substantial, the BT inverse cascade is better represented and energy is dissipated through bottom drag at larger spatial scales. When considering the domain-wide distribution of barotropization, we observe the strongest barotropization with resolution in the northern hemisphere. The vertical structure and KE partitioning in the ACC is less sensitive to increased resolution due to the influence of the mean flow and standing meanders.

An important finding of our work is that the BT to BC eddy KE ratio is a useful metric in assessing vertical structure of the flow and mesoscale eddy effects. The next objective is to develop a theory to explain the BT/BC eddy KE partitioning (and how it relates to the mean flow) to guide vertical structure choices in parameterizing eddy-driven barotropization. Much of the existing literature on vertical structure in this regard has considered two-layer QG systems. Larichev and Held (1995) derive a scaling for the ratio V/U, where V is BT rms eddy velocity and U is BC mean thermal wind, as

$$\frac{V}{U} \approx \frac{R_\mathrm{E}}{R_\mathrm{D}}. \tag{22}$$

This result is for an f-plane, and states that the partitioning between BT and BC modes is linearly related to the ratio of the eddy scale (set by domain size) and the deformation radius. Larger $R_\mathrm{E}/R_\mathrm{D}$ indicates a more extensive BT inverse cascade and stronger BT flow. Our result (Figure 14) is that the ratio of V^2/U^2 (KE rather than velocities) scales with $R_\mathrm{E}/R_\mathrm{D}$ (with the caveat that our energy-containing scale calculation was challenged by the relatively small horizontal extent of the NeverWorld2 domain and the importance of β at lower latitudes). In a later work Held and Larichev (1996) consider a β-plane where the barotropic cascade is arrested by the β-effect at the Rhines scale ($R_\mathrm{Rhines} = \sqrt{V/\beta}$). The scaling is modified to:

$$\frac{V}{U} \approx \frac{R_\mathrm{Rhines}}{R_\mathrm{D}}. \tag{23}$$

Subsequent studies by Lapeyre and Held (2003), Thompson and Young (2006, 2007), and Chang and Held (2019, 2021) have built upon these results to refine theories for meridional eddy diffusivity incorporating frictional effects and considering the role of β. However, the influences of such factors on BT/BC velocity partitioning were not considered beyond the original works of Larichev and Held. When parameterizing eddy effects on momentum and energetics, particularly from a vertical structure standpoint, understanding the mechanisms governing BT/BC eddy KE partitioning remains a theoretical gap.

Recently, Gallet and Ferrari (2020) and Gallet and Ferrari (2021) considered mechanisms by which the inverse cascade is arrested on an f- and β-plane (respectively). Two regimes emerge: 'vortex gas', with f-plane dynamics consistent with Larichev and Held (1995), and 'zonostrophic', characterized by β-plane dynamics as in Held and Larichev (1996). In the vortex gas regime, the inverse cascade is arrested through bottom friction and we can imagine that the BT/BC eddy KE ratio is governed by $R_\mathrm{E}/R_\mathrm{D}$. In the zonostrophic regime, the cascade is halted by jet formation and it is possible that $V/U \approx R_\mathrm{Rhines}/R_\mathrm{D}$ holds. The transition between these two regimes is governed by the parameter $B = L_0^2/L_\mathrm{Rhines}^2$, where L_0 is the peak of the BT spectrum (Gallet & Ferrari, 2021). Yet, there remains a significant gap between theoretical two-layer QG findings on vertical structure and realistic ocean model/GCM eddy representation.

The study yields insights useful to improving existing parameterizations through incorporating vertical structure effects of mesoscale eddies. An important advance in mesoscale eddy schemes involves reinjecting kinetic energy into the resolved flow through a backscatter formulation (Bachman, 2019; Jansen et al., 2020; Juricke et al., 2020). Backscatter is intended to parameterize an important component of the eddy energy cycle: the return of eddy KE that should result from the slumping of isopycnals by baroclinic instability to the resolved flow. The results presented here show that KE distribution across vertical modes shifts towards high baroclinic modes when eddies are poorly resolved. To mitigate this issue, KE may be reinjected in a way that leads to more energy in the BT or graver modes. Future work involves testing existing eddy parameterization schemes, including present formulations of backscatter. Based on how existing schemes perform in capturing the metrics considered here, we will seek improvements to vertical structure representation of mesoscale eddy effects.

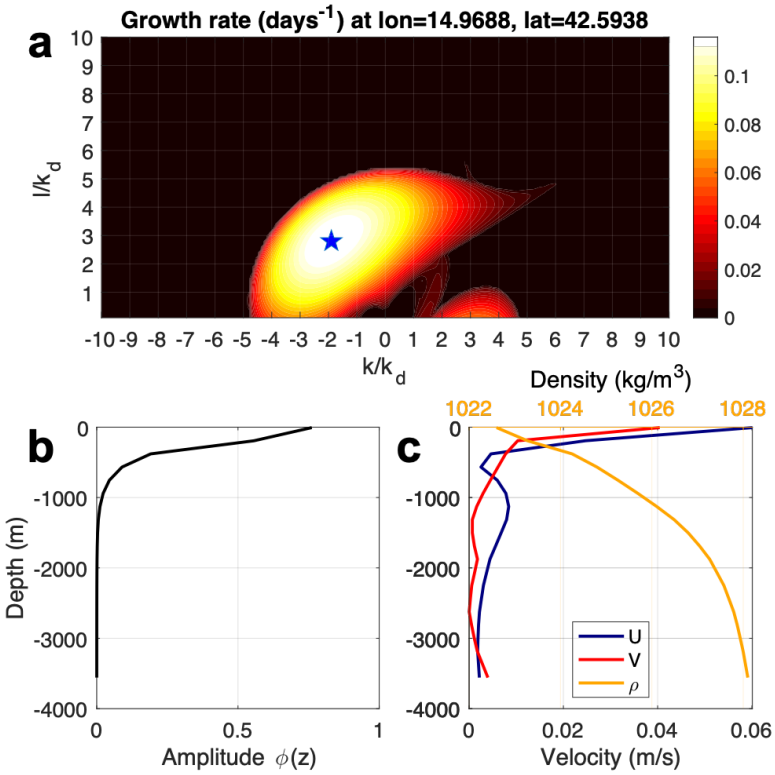

Figure A1. Computation of the fastest-growing QG instability mode at a northwestern point in the 1/32° NeverWorld2 domain as indicated in Figure 1b: (a) growth rates as functions of the ratio of zonal and meridional wavenumber (k, l respectively) to the first deformation wavenumber k_d (the star indicates the fastest growing mode); (b) amplitude of the fastest growing mode as a function of depth; and (c) the 500-day mean stratification and velocities as a function of depth at this location.

Appendix A Linear QG instability analysis as a metric for resolution

We consider a second metric for eddy resolution by computing the wavelength of the fastest-growing mode, R_{MAX}, using linear stability analysis. Though the deformation scale R_{D} is the fastest growing instability lengthscale in the simplest models of baroclinic instability (e.g. Eady and Phillips), S. Smith (2007) found that when performing local instability analysis of the oceanic mean state R_{MAX} is often significantly smaller than R_{D}. To capture the formation and development of mesoscale eddies, one may therefore need to go beyond resolving the deformation radius. We will use this metric to ask whether accurately representing vertical structure hinges upon resolving R_{MAX} or whether R_{D} is sufficient.

Application of the linear stability calculation regionally is detailed, for example, in S. Smith (2007). We summarize it here, using continuous z-coordinates — note that a standard centered vertical differencing with $\Delta z = h_k$ is isomorphic to an isopycnal calculation (Pedlosky, 1987). The linearized, inviscid QG potential vorticity equation is

$$\frac{\partial q}{\partial t} + \mathbf{U} \cdot \nabla q + \beta v = 0, \tag{A1}$$

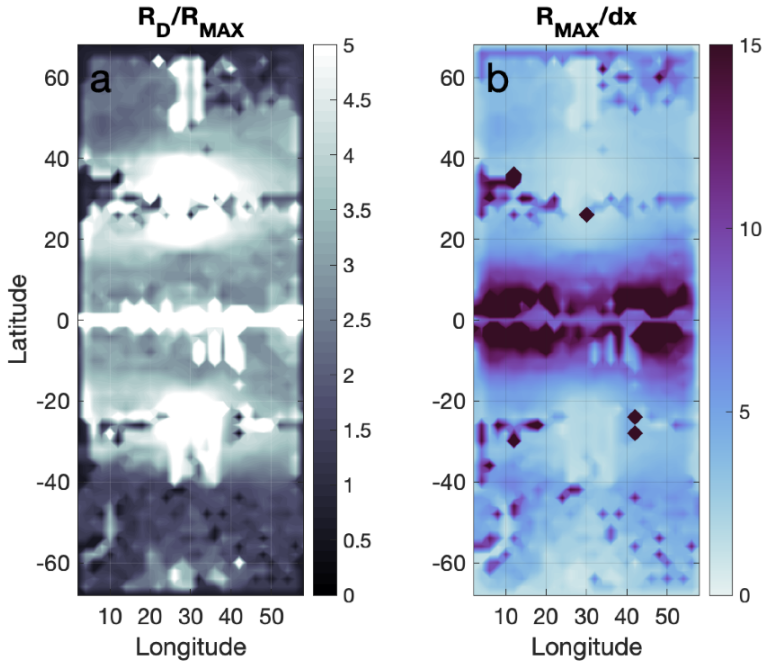

Figure A2. Domain-wide results from the fastest-growing QG instability mode calculation for the 1/32° NeverWorld2: (a) ratio of the deformation radius, R_{D}, to the lengthscale of the fastest growing instability mode, R_{MAX}; (b) $R_{\mathrm{MAX}}/\Delta x$, analogous to Figure 3.

where $q = \nabla^2\psi + \frac{d}{dz}\left(\frac{f^2}{N^2}\frac{d\psi}{dz}\right)$ is the QG potential vorticity, ψ is the horizontal streamfunction, and $\mathbf{U} = (U(z), V(z))$ and $N^2(z)$ are the mean state characterized by slowly-varying horizontal flow that depends only on z. A plane wave solution of the form $\psi = \hat{\psi}(z)e^{i(kx+ly-\omega t)}$ (where $\hat{\psi}$ is complex amplitude, k and l and zonal and meridional wavenumbers, and ω is frequency) is substituted into (A1), forming an eigenvalue problem for the normal modes $\hat{\psi}(z)$ (eigenvectors) and frequencies ω (eigenvalues). An imaginary ω corresponds to a growing instability, so the imaginary component of ω is computed for a range of k, l and the wavenumber of the maximum growth rate is identified. An example of such a calculation is shown in Figure A1. The result of the calculation shows that $R_{\mathrm{MAX}} \sim (1/2)R_{\mathrm{D}}$ at this location. The vertical structure of the most unstable mode is surface intensified with one zero crossing. The computation was performed for the entire domain for the 1/32° case (Figure A2). Here R_{MAX} is 2 to 3 times smaller than R_{D} in the higher latitudes, and 3 to 5 times smaller over the parts of the topographic ridge and within the midlatitude gyres. When considering how well the 1/32° case resolves R_{MAX}, we see that the simulation is broadly eddy resolving but the midlatitude gyres and boundaries exhibit smaller-scale instabilities that may not be fully captured.

Appendix B Projecting energy onto vertical modes

To project model fields onto vertical modes, we first interpolate the velocity and isopycnal displacement locally onto a uniform grid in z, and then interpret these as discretized approximations of continuous functions. See Wunsch and Stammer (1997) for a recent reference. Then we may introduce the standard vertical modes $F_m(z)$, which

are solutions to the equation

$$\frac{\mathrm{d}}{\mathrm{d}z}\left(\frac{f^2}{N^2}\frac{\mathrm{d}F_m}{\mathrm{d}z}\right) + \lambda_m^2 F_m = 0 \quad \text{with} \quad \frac{\mathrm{d}F_m}{\mathrm{d}z} = 0 \text{ at } z = 0, -D. \tag{B1}$$

The eigenfunctions F_m form a complete orhtogonal basis onto which functions that satisfy the same Neumann boundary conditions may be projected. The eigenvalues λ_m, with $m = 0, 1, 2, \ldots$ are the deformation wavenumbers, with units inverse length. Note that $m = 0$ is the barotropic mode, with $\lambda_0 = 0$, and $m = 1$ is the first baroclinic mode, with $\lambda_1 = 1/R_\mathrm{D}$. We define F_m as dimensionless, and normalize them so that they satisfy the orthogonality conditions

$$\frac{1}{D}\int_{-D}^{0} F_n F_m \,\mathrm{d}z = \delta_{mn}. \tag{B2}$$

The horizontal velocity components at each point may be expanded a linear combination of M modes

$$\mathbf{u}(z) = \sum_{m=1}^{M} \tilde{\mathbf{u}}_m F_m(z), \tag{B3}$$

where an over-tilde denotes the mode amplitudes, and $\tilde{\mathbf{u}}_m$ has the units of velocity. Using the orthogonality condition, the kinetic energy is then

$$K = \sum_{m=1}^{M} K_m, \quad \text{where} \quad K_m \equiv \frac{|\tilde{\mathbf{u}}_m|^2}{2} \tag{B4}$$

is the kinetic energy in mode m at wavenumber λ_m.

For potential energy, note that in z-coordinates, the displacement field $\eta = b/N^2$, where $b = -g\Delta\rho/\rho_0$ is the buouyancy and $N^2 = g'/\Delta z$. The potential energy is then

$$P = \frac{1}{2D}\int_{-D}^{0} \frac{b^2}{N^2}\,\mathrm{d}z. \tag{B5}$$

With the approximation $\eta|_{z=0} = \eta|_{z=-D} = 0$ (flat bottom, rigid lid), the buoyancy may be projected onto the derivatives of the modes $F_m(z)$ as

$$b = \sum_{m=1}^{M} \tilde{\alpha}_m \frac{\mathrm{d}F_m}{\mathrm{d}z}, \tag{B6}$$

where because F_m is dimensionless and b has dimensions of an acceleration, $\tilde{\alpha}_m$ must have dimensions of squared velocity. The potential energy is then

$$\begin{aligned} P &= \frac{1}{2D}\sum_{mn} \tilde{\alpha}_m \tilde{\alpha}_n \int_{-D}^{0} \frac{1}{N^2}\frac{\mathrm{d}F_m}{\mathrm{d}z}\frac{\mathrm{d}F_n}{\mathrm{d}z}\,\mathrm{d}z \\ &= \sum_m P_m, \quad \text{where} \quad P_m \equiv \frac{\lambda_m^2 \tilde{\alpha}_m^2}{2f^2} \end{aligned} \tag{B7}$$

is the APE in mode m at wavenumber λ_m. In the calculation of (B7), we used integration by parts, substition from (B1), and the orthogonality condition (B2).

The spectra of K_m and P_m are shown in Figure 12.

Open Research

The Jupyter notebooks used to generate figures in the manuscript are available at https://doi.org/10.5281/zenodo.6558379. The NeverWorld2 configuration used in this manuscript is detailed in Marques et al. (2022). The MOM6 source code and NeverWorld2

configuration files are available at https://doi.org/10.5281/zenodo.6462289. As stated in the previous reference, the NeverWorld2 dataset (including initial conditions and restart files) will be made publicly available via Open Storage Network.

Acknowledgments

We thank Nora Loose, Gustavo Marques, Jacob Steinberg, Chiung-Yin Chang, Neeraja Bhamidipati, and the other members of the Ocean Transport and Eddy Energy Climate Process Team for insightful discussions, sharing code, and for their support throughout the course of this project. EY, LZ, and SS were supported by NSF grant OCE 1912357 and NOAA CVP NA19OAR4310364.

References

Adcroft, A., Anderson, W., Balaji, V., Blanton, C., Bushuk, M., Dufour, C. O., ... Zhang, R. (2019). The gfdl global ocean and sea ice model om4.0: Model description and simulation features. *Journal of Advances in Modeling Earth Systems*, *11*(10), 3167-3211. doi: https://doi.org/10.1029/2019MS001726

Bachman, S. D. (2019). The GM+ E closure: a framework for coupling backscatter with the Gent and McWilliams parameterization. *Ocean Modelling*, *136*, 85–106.

Cessi, P. (2008, August). An energy-constrained parameterization of eddy buoyancy flux. *Journal of Physical Oceanography*, *38*(8), 1807–1819. (Publisher: American Meteorological Society Section: Journal of Physical Oceanography) doi: 10.1175/2007JPO3812.1

Chang, C.-Y., & Held, I. M. (2019, June). The Control of Surface Friction on the Scales of Baroclinic Eddies in a Homogeneous Quasigeostrophic Two-Layer Model. *Journal of the Atmospheric Sciences*, *76*(6), 1627–1643. (Publisher: American Meteorological Society Section: Journal of the Atmospheric Sciences) doi: 10.1175/JAS-D-18-0333.1

Chang, C.-Y., & Held, I. M. (2021, January). The Parameter Dependence of Eddy Heat Flux in a Homogeneous Quasigeostrophic Two-Layer Model on a beta-Plane with Quadratic Friction. *Journal of the Atmospheric Sciences*, *78*(1), 97–106. (Publisher: American Meteorological Society Section: Journal of the Atmospheric Sciences) doi: 10.1175/JAS-D-20-0145.1

Charney, J. G. (1971). Geostrophic turbulence. *Journal of Atmospheric Sciences*, *28*(6), 1087 - 1095. doi: 10.1175/1520-0469(1971)028⟨1087:GT⟩2.0.CO;2

Chemke, R., & Kaspi, Y. (2016). The latitudinal dependence of the oceanic barotropic eddy kinetic energy and macroturbulence energy transport. *Geophysical Research Letters*, *43*(6), 2723-2731. doi: https://doi.org/10.1002/2016GL067847

de La Lama, M. S., LaCasce, J. H., & Fuhr, H. K. (2016, January). The vertical structure of ocean eddies. *Dynamics and Statistics of the Climate System*, *1*(1). doi: 10.1093/climsys/dzw001

Eady, E. T. (1949). Long Waves and Cyclone Waves. *Tellus*, *1*(3), 33–52. doi: 10.1111/j.2153-3490.1949.tb01265.x

Eden, C., & Greatbatch, R. J. (2008, January). Towards a mesoscale eddy closure. *Ocean Modelling*, *20*(3), 223–239. doi: 10.1016/j.ocemod.2007.09.002

Ferrari, R., & Wunsch, C. (2009). Ocean circulation kinetic energy: Reservoirs, sources, and sinks. *Annual Review of Fluid Mechanics*, *41*(1), 253-282. doi: 10.1146/annurev.fluid.40.111406.102139

Fu, L.-L., & Flierl, G. R. (1980). Nonlinear energy and enstrophy transfers in a realistically stratified ocean. *Dynamics of Atmospheres and Oceans*, *4*(4), 219–246. doi: https://doi.org/10.1016/0377-0265(80)90029-9

Gallet, B., & Ferrari, R. (2020, March). The vortex gas scaling regime of baroclinic turbulence. *Proceedings of the National Academy of Sciences*, *117*(9), 4491–

4497. (Publisher: National Academy of Sciences Section: Physical Sciences) doi: 10.1073/pnas.1916272117

Gallet, B., & Ferrari, R. (2021). A Quantitative Scaling Theory for Meridional Heat Transport in Planetary Atmospheres and Oceans. *AGU Advances*, *2*(3), e2020AV000362. (_eprint: https://onlinelibrary.wiley.com/doi/pdf/10.1029/2020AV000362) doi: 10.1029/2020AV000362

Gent, P. R., Willebrand, J., McDougall, T. J., & McWilliams, J. C. (1995, April). Parameterizing Eddy-Induced Tracer Transports in Ocean Circulation Models. *Journal of Physical Oceanography*, *25*(4), 463–474. (Publisher: American Meteorological Society Section: Journal of Physical Oceanography) doi: 10.1175/1520-0485(1995)025⟨0463:PEITTI⟩2.0.CO;2

Gill, A. E., Green, J. S. A., & Simmons, A. J. (1974). Energy partition in the large-scale ocean circulation and the production of mid-ocean eddies. *Deep Sea Research and Oceanographic Abstracts*, *21*(7), 499–528. doi: https://doi.org/10.1016/0011-7471(74)90010-2

Griffies, S. M., & Hallberg, R. W. (2000, August). Biharmonic friction with a Smagorinsky-like viscosity for use in large-scale eddy-permitting ocean models. *Monthly Weather Review*, *128*(8), 2935–2946. (Publisher: American Meteorological Society) doi: 10.1175/1520-0493(2000)128⟨2935:BFWASL⟩2.0.CO;2

Griffies, S. M., Winton, M., Anderson, W. G., Benson, R., Delworth, T. L., Dufour, C. O., ... Zhang, R. (2015, February). Impacts on Ocean Heat from Transient Mesoscale Eddies in a Hierarchy of Climate Models. *Journal of Climate*, *28*(3), 952–977. Retrieved from `https://journals.ametsoc.org/view/journals/clim/28/3/jcli-d-14-00353.1.xml` (Publisher: American Meteorological Society Section: Journal of Climate) doi: 10.1175/JCLI-D-14-00353.1

Grooms, I., Loose, N., Abernathey, R., Steinberg, J., Bachman, S. D., Marques, G., ... Yankovsky, E. (2021, March). *Diffusion-based smoothers for spatial filtering of gridded geophysical data* [preprint]. (Archive Location: world Publisher: Earth and Space Science Open Archive Section: Informatics) doi: 10.1002/essoar.10506591.1

Hallberg, R. (2013, December). Using a resolution function to regulate parameterizations of oceanic mesoscale eddy effects. *Ocean Modelling*, *72*, 92–103. doi: 10.1016/j.ocemod.2013.08.007

Held, I. M., & Larichev, V. D. (1996, April). A Scaling Theory for Horizontally Homogeneous, Baroclinically Unstable Flow on a Beta Plane. *Journal of the Atmospheric Sciences*, *53*(7), 946–952. (Publisher: American Meteorological Society Section: Journal of the Atmospheric Sciences) doi: 10.1175/1520-0469(1996)053⟨0946:ASTFHH⟩2.0.CO;2

Honnert, R., Efstathiou, G. A., Beare, R. J., Ito, J., Lock, A., Neggers, R., ... Zhou, B. (2020). The atmospheric boundary layer and the "gray zone" of turbulence: A critical review. *Journal of Geophysical Research: Atmospheres*, *125*(13). doi: 10.1029/2019JD030317

Jansen, M. F., Adcroft, A., Khani, S., & Kong, H. (2020). Toward an energetically consistent, resolution aware parameterization of ocean mesoscale eddies. *Journal of Advances in Modeling Earth Systems*, *11*(8), 2844-2860.

Jansen, M. F., & Held, I. M. (2014, August). Parameterizing subgrid-scale eddy effects using energetically consistent backscatter. *Ocean Modelling*, *80*, 36–48. doi: 10.1016/j.ocemod.2014.06.002

Juricke, S., Danilov, S., Koldunov, N., Oliver, M., & Sidorenko, D. (2020). Ocean Kinetic Energy Backscatter Parametrization on Unstructured Grids: Impact on Global Eddy-Permitting Simulations. *Journal of Advances in Modeling Earth Systems*, *12*(1). doi: 10.1029/2019MS001855

Kjellsson, J., & Zanna, L. (2017, September). The impact of horizontal resolution on energy transfers in global ocean models. *Fluids*, *2*(3), 45. (Num-

ber: 3 Publisher: Multidisciplinary Digital Publishing Institute) doi: 10.3390/fluids2030045

Kraichnan, R. H. (1967, July). Inertial ranges in two-dimensional turbulence. *The Physics of Fluids*, *10*(7), 1417–1423. (Publisher: American Institute of Physics) doi: 10.1063/1.1762301

Lapeyre, G., & Held, I. M. (2003, December). Diffusivity, Kinetic Energy Dissipation, and Closure Theories for the Poleward Eddy Heat Flux. *Journal of the Atmospheric Sciences*, *60*(23), 2907–2916. (Publisher: American Meteorological Society Section: Journal of the Atmospheric Sciences) doi: 10.1175/1520-0469(2003)060⟨2907:DKEDAC⟩2.0.CO;2

Larichev, V. D., & Held, I. M. (1995, October). Eddy amplitudes and fluxes in a homogeneous model of fully developed baroclinic instability. *Journal of Physical Oceanography*, *25*(10), 2285–2297. (Publisher: American Meteorological Society Section: Journal of Physical Oceanography) doi: 10.1175/1520-0485(1995)025⟨2285:EAAFIA⟩2.0.CO;2

Loose, N., Abernathey, R., Grooms, I., Busecke, J., Guillaumin, A., Yankovsky, E., ... Martin, P. (2022, February). GCM-Filters: A Python Package for Diffusion-based Spatial Filtering of Gridded Data. *Journal of Open Source Software*, *7*(70), 3947. doi: 10.21105/joss.03947

Marques, G., Loose, N., Adcroft, A., Yankovsky, E., Steinberg, J., Griffies, S., ... Chang, C.-Y. (2022, August). *NeverWorld2: An idealized model hierarchy to investigate ocean mesoscale eddies across resolutions* [preprint]. (Archive Location: world Publisher: Earth and Space Science Open Archive Section: Oceanography) doi: 10.1002/essoar.10511043.1

Marshall, D. P., & Adcroft, A. J. (2010, January). Parameterization of ocean eddies: Potential vorticity mixing, energetics and Arnold's first stability theorem. *Ocean Modelling*, *32*(3), 188–204. doi: 10.1016/j.ocemod.2010.02.001

Marshall, D. P., Maddison, J. R., & Berloff, P. S. (2012, April). A Framework for Parameterizing Eddy Potential Vorticity Fluxes. *Journal of Physical Oceanography*, *42*(4), 539–557. (Publisher: American Meteorological Society Section: Journal of Physical Oceanography) doi: 10.1175/JPO-D-11-048.1

Pedlosky, J. (1987). *Geophysical fluid dynamics* (2nd ed.). New York: Springer. (Pages: 710)

Porta Mana, P., & Zanna, L. (2014, July). Toward a stochastic parameterization of ocean mesoscale eddies. *Ocean Modelling*, *79*, 1–20. doi: 10.1016/j.ocemod.2014.04.002

Rhines, P. (1977). The dynamics of unsteady currents. *The Sea*, *6*, 189–318. (Publisher: Wiley Interscience)

Salmon, R. (1978). Two-layer quasi-geostrophic turbulence in a simple special case. *Geophysical & Astrophysical Fluid Dynamics*, *10*(1), 25-52. doi: 10.1080/03091927808242628

Smith, K. S., & Vallis, G. K. (2001, February). The scales and equilibration of midocean eddies: Freely evolving flow. *Journal of Physical Oceanography*, *31*(2), 554–571. (Publisher: American Meteorological Society Section: Journal of Physical Oceanography) doi: 10.1175/1520-0485(2001)031⟨0554:TSAEOM⟩2.0.CO;2

Smith, S. (2007, 09). The geography of linear baroclinic instability in earth's oceans. *Journal of Marine Research*, *65*, 655-683. doi: 10.1357/002224007783649484

Stanley, Z., Bachman, S. D., & Grooms, I. (2020). Vertical Structure of Ocean Mesoscale Eddies with Implications for Parameterizations of Tracer Transport. *Journal of Advances in Modeling Earth Systems*, *12*(10), e2020MS002151. doi: 10.1029/2020MS002151

Thompson, A. F., & Young, W. R. (2006, April). Scaling Baroclinic Eddy Fluxes: Vortices and Energy Balance. *Journal of Physical Oceanography*, *36*(4), 720–738. (Publisher: American Meteorological Society Section: Journal of Physical

765 Oceanography) doi: 10.1175/JPO2874.1
766 Thompson, A. F., & Young, W. R. (2007, September). Two-Layer Baroclinic Eddy
767 Heat Fluxes: Zonal Flows and Energy Balance. *Journal of the Atmospheric*
768 *Sciences*, *64*(9), 3214–3231. Retrieved from `https://journals.ametsoc.org/`
769 `view/journals/atsc/64/9/jas4000.1.xml` (Publisher: American Me-
770 teorological Society Section: Journal of the Atmospheric Sciences) doi:
771 10.1175/JAS4000.1
772 Treguier, A. M., Held, I. M., & Larichev, V. D. (1997, April). Parameteri-
773 zation of Quasigeostrophic Eddies in Primitive Equation Ocean Models.
774 *Journal of Physical Oceanography*, *27*(4), 567–580. (Publisher: American
775 Meteorological Society Section: Journal of Physical Oceanography) doi:
776 10.1175/1520-0485(1997)027⟨0567:POQEIP⟩2.0.CO;2
777 Tulloch, R., Marshall, J., Hill, C., & Smith, K. S. (2011, June). Scales, growth rates,
778 and spectral fluxes of baroclinic instability in the ocean. *Journal of Physical*
779 *Oceanography*, *41*(6), 1057–1076. (Publisher: American Meteorological Society
780 Section: Journal of Physical Oceanography) doi: 10.1175/2011JPO4404.1
781 Wunsch, C. (1997, August). The vertical partition of oceanic horizontal kinetic en-
782 ergy. *Journal of Physical Oceanography*, *27*(8), 1770–1794. (Publisher: Ameri-
783 can Meteorological Society Section: Journal of Physical Oceanography) doi: 10
784 .1175/1520-0485(1997)027⟨1770:TVPOOH⟩2.0.CO;2
785 Wunsch, C., & Stammer, D. (1997). Atmospheric loading and the oceanic "in-
786 verted barometer" effect. *Reviews of Geophysics*, *35*(1), 79–107. doi: 10.1029/
787 96RG03037
788 Zanna, L., Porta Mana, P., Anstey, J., David, T., & Bolton, T. (2017, March).
789 Scale-aware deterministic and stochastic parametrizations of eddy-mean flow
790 interaction. *Ocean Modelling*, *111*, 66–80. doi: 10.1016/j.ocemod.2017.01.004

Figure 1.

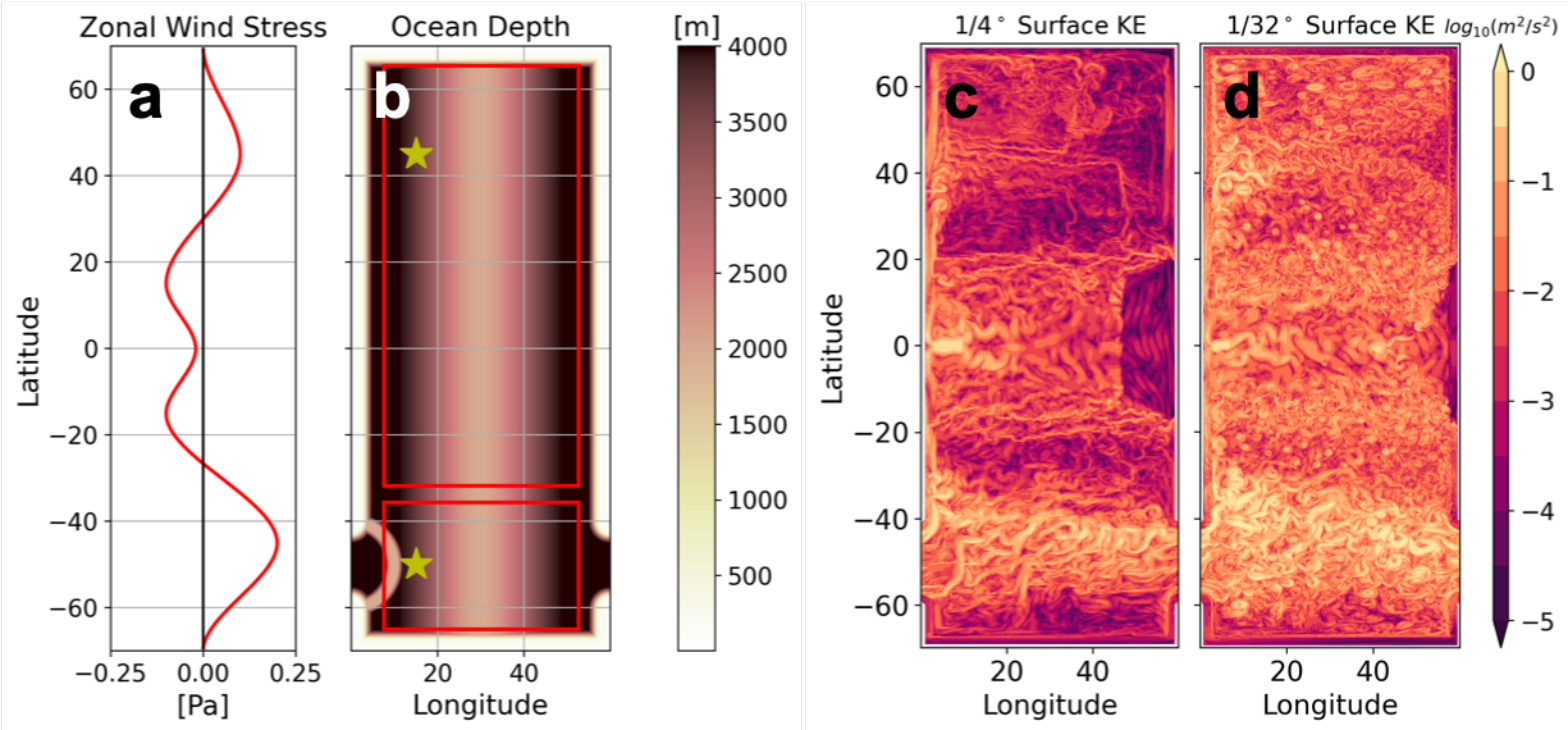
Zonal Wind Stress
Ocean Depth
[m]
a
b
c
d
1/4 ° Surface KE
1/32 ° Surface KE $log_{10}(m^2/s^2)$
Latitude
Longitude
[Pa]
60
40
20
0
−20
−40
−60
−0.25
0.00
0.25
4000
3500
3000
2500
2000
1500
1000
500
−1
−2
−3
−4
−5

Figure 2.

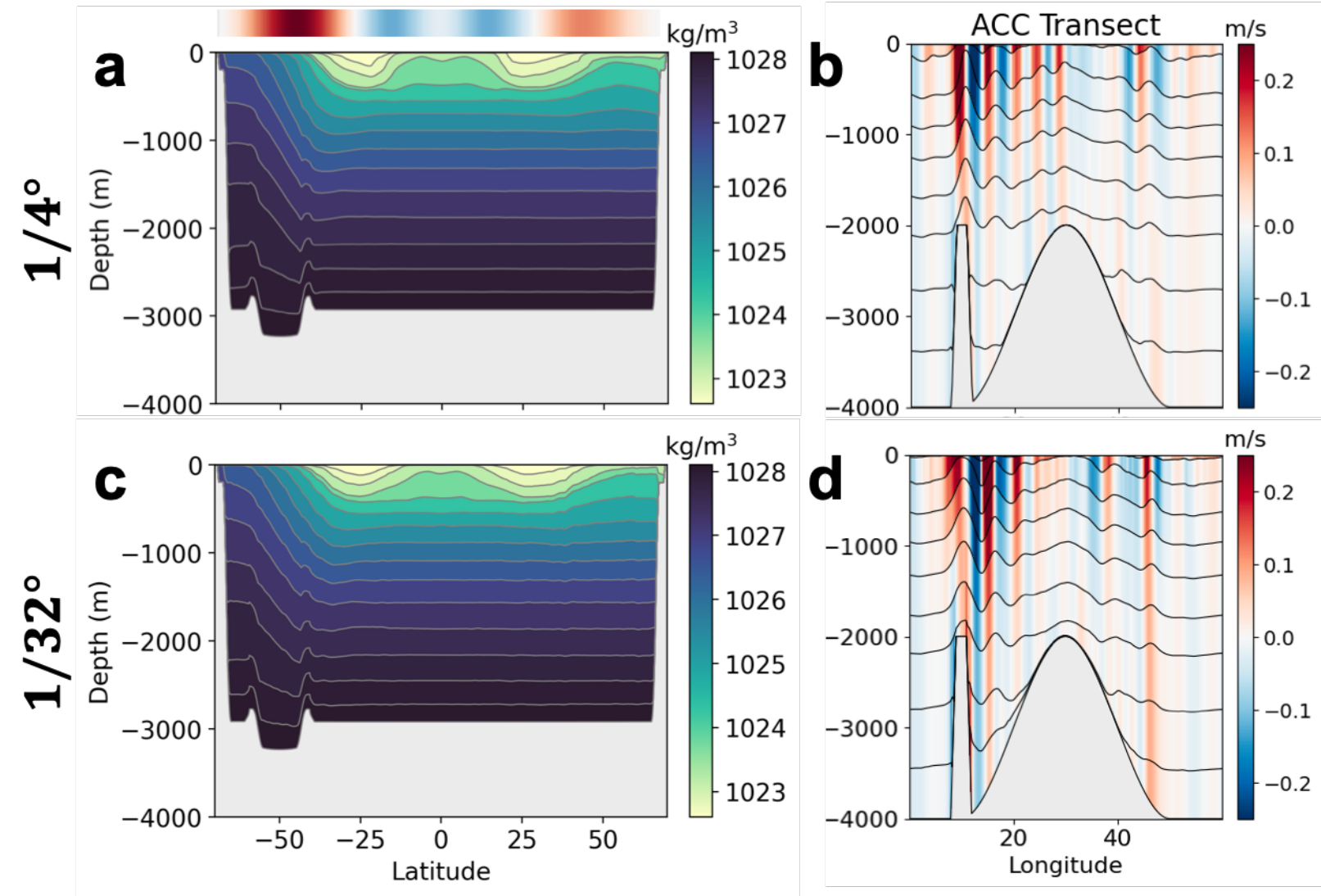
1/4°
1/32°
a
b
c
d
ACC Transect
kg/m³
m/s
Depth (m)
Latitude
Longitude
0
−1000
−2000
−3000
−4000
1028
1027
1026
1025
1024
1023
0.2
0.1
0.0
−0.1
−0.2
−50
−25
0
25
50
20
40

Figure 3.

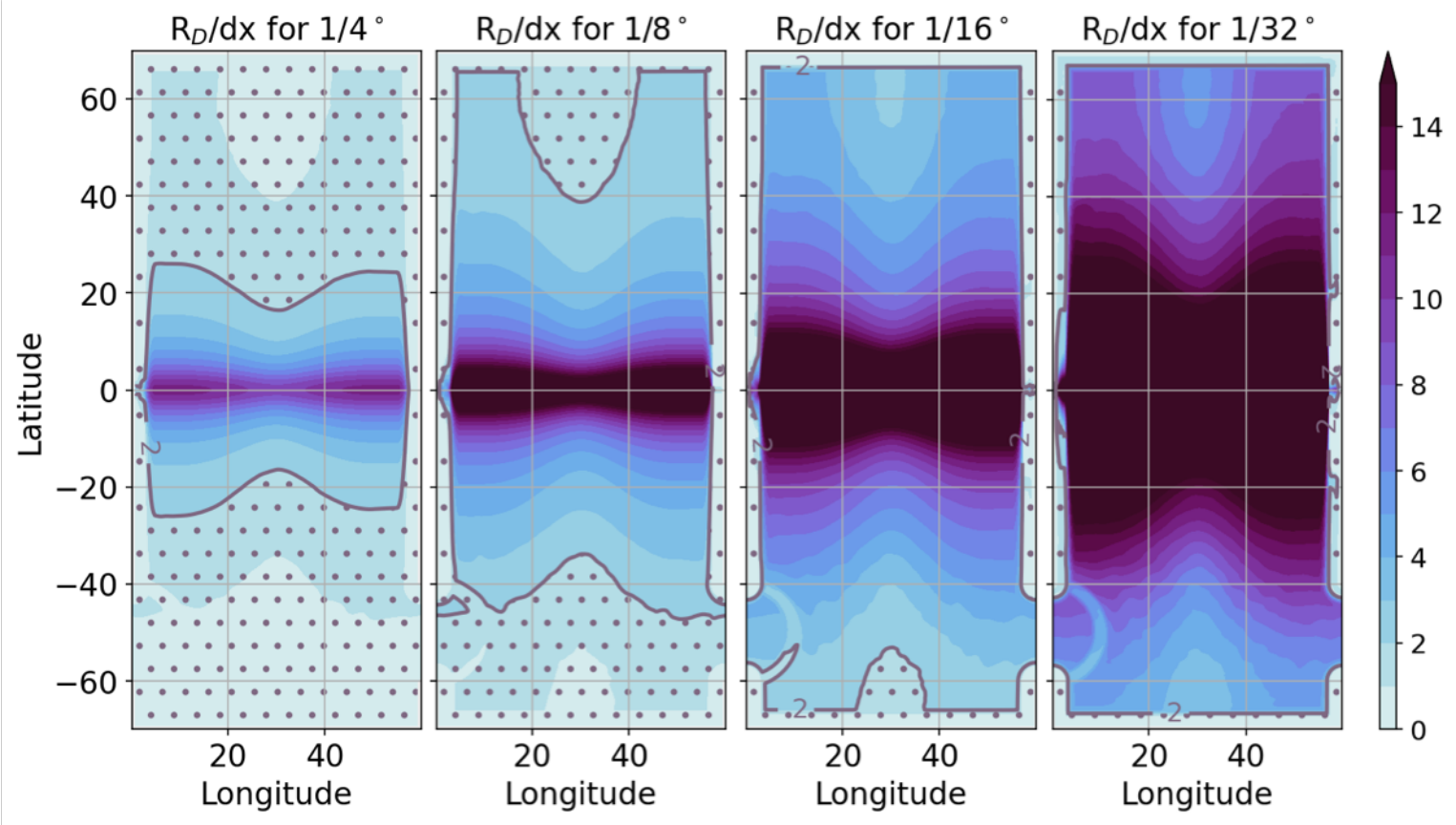
R_D/dx for 1/4 °
R_D/dx for 1/8 °
R_D/dx for 1/16 °
R_D/dx for 1/32 °
Latitude
60
40
20
0
−20
−40
−60
20
40
Longitude
2
14
12
10
8
6
4
2
0

Figure 4.

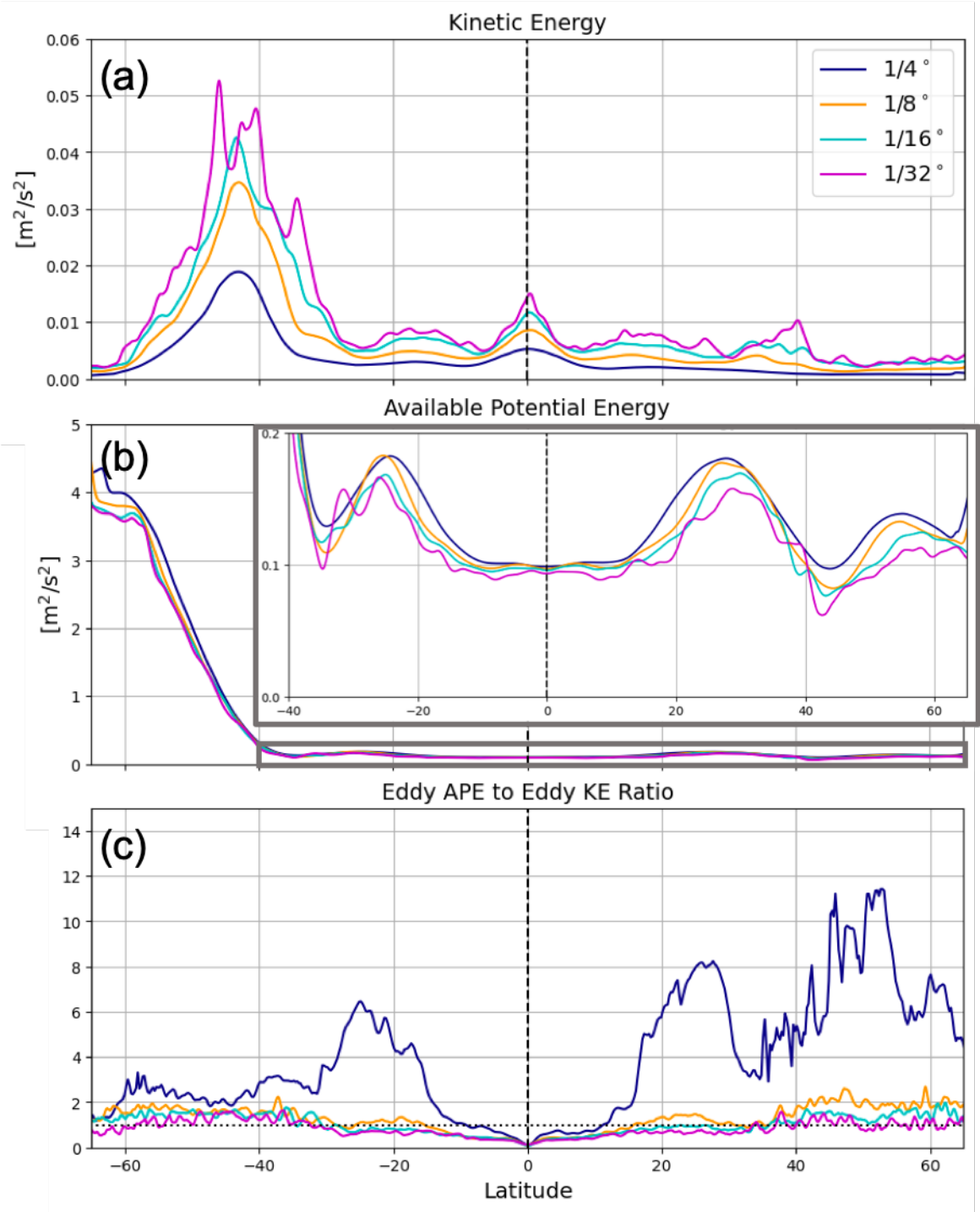
Kinetic Energy
(a)
1/4 °
1/8 °
1/16 °
1/32 °
[m²/s²]
0.06
0.05
0.04
0.03
0.02
0.01
0.00
Available Potential Energy
(b)
[m²/s²]
5
4
3
2
1
0
0.2
0.1
0.0
−40
−20
0
20
40
60
Eddy APE to Eddy KE Ratio
(c)
14
12
10
8
6
4
2
0
−60
−40
−20
0
20
40
60
Latitude

Figure 5.

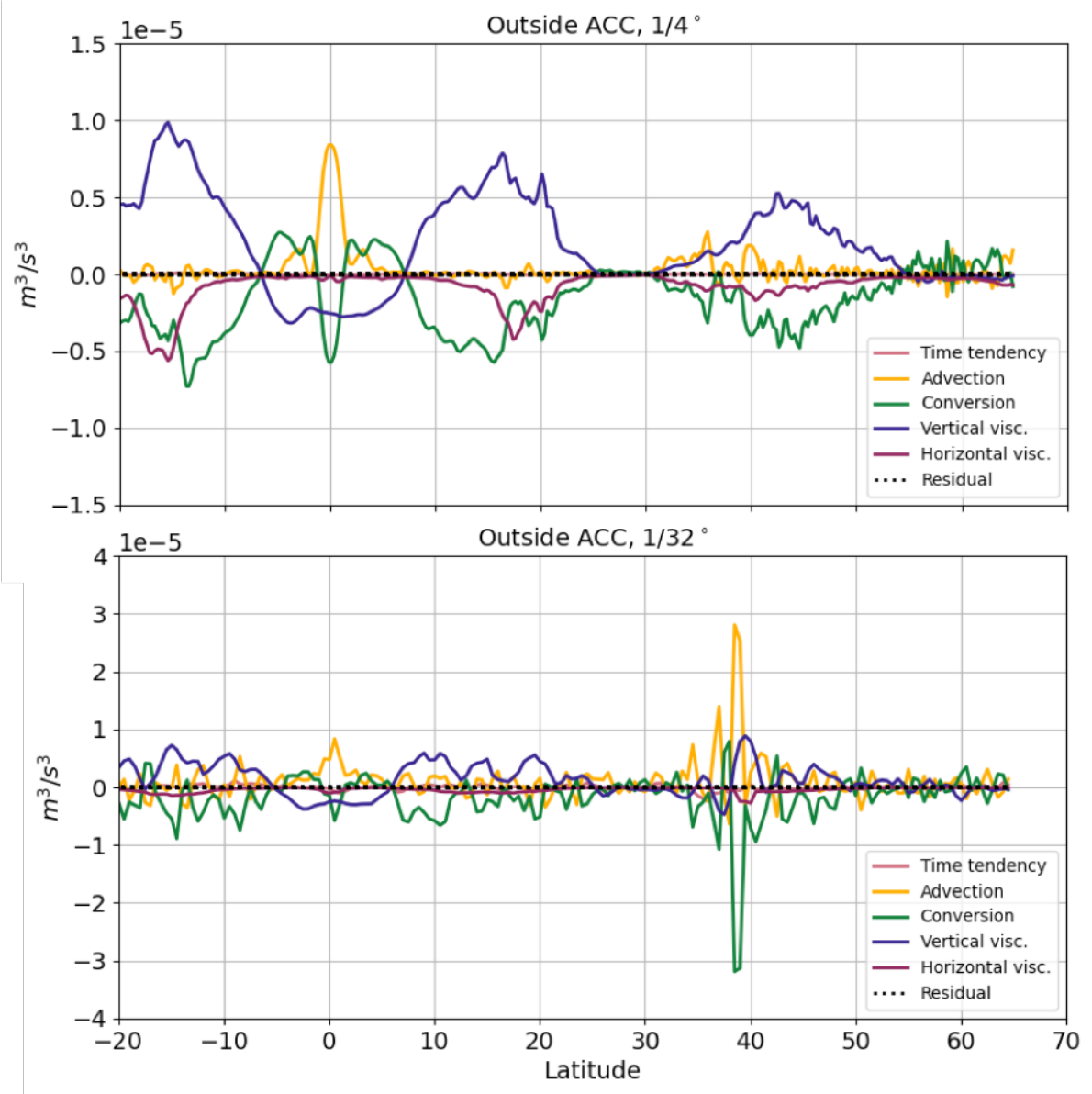
Outside ACC, 1/4°
1e−5
1.5
1.0
0.5
0.0
−0.5
−1.0
−1.5
m^3/s^3
Time tendency
Advection
Conversion
Vertical visc.
Horizontal visc.
Residual
Outside ACC, 1/32°
1e−5
4
3
2
1
0
−1
−2
−3
−4
m^3/s^3
Time tendency
Advection
Conversion
Vertical visc.
Horizontal visc.
Residual
−20
−10
0
10
20
30
40
50
60
70
Latitude

Figure 6.

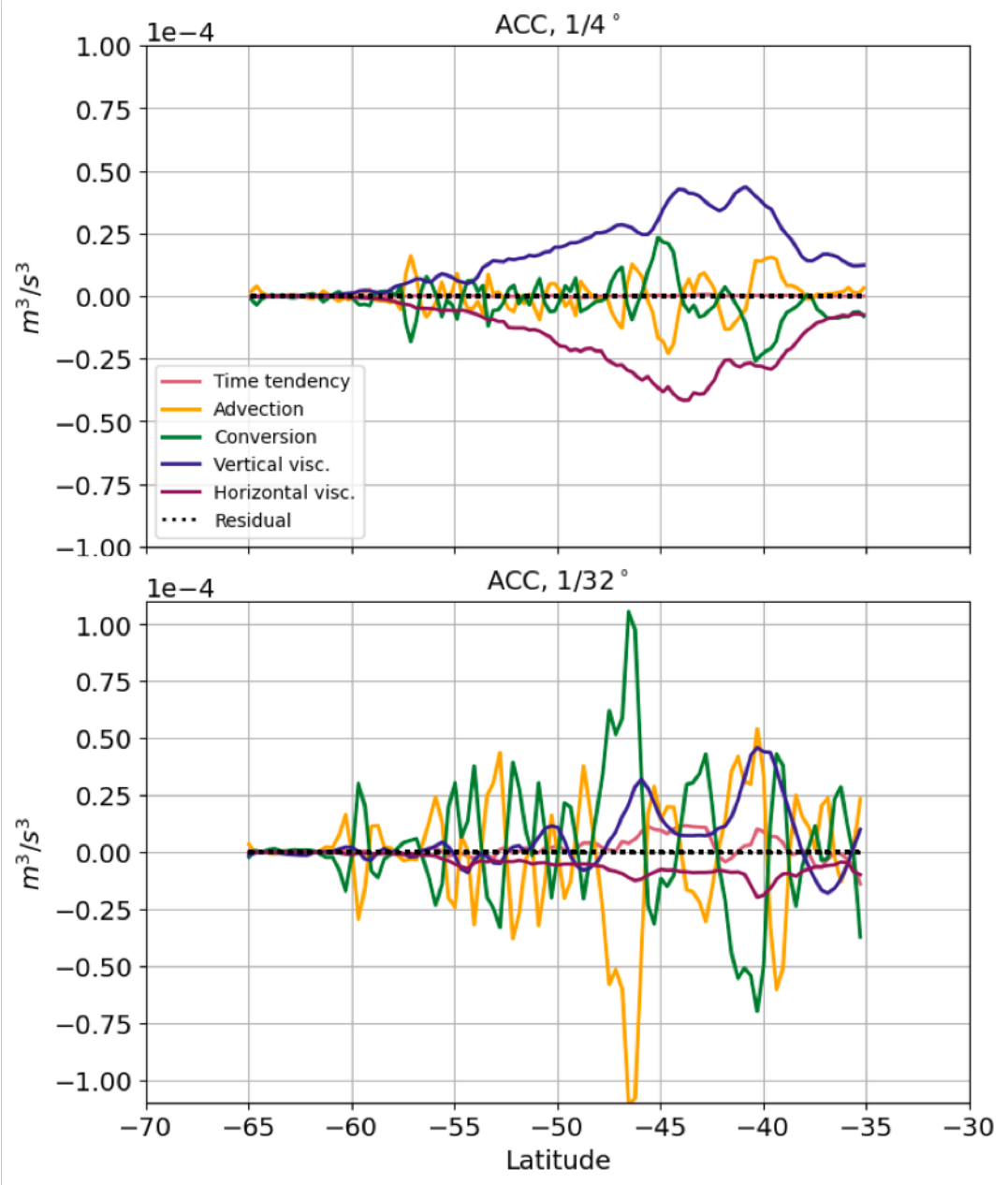
ACC, 1/4 °
1e−4
1.00
0.75
0.50
0.25
0.00
−0.25
−0.50
−0.75
−1.00
m^3/s^3
Time tendency
Advection
Conversion
Vertical visc.
Horizontal visc.
Residual
ACC, 1/32 °
1e−4
1.00
0.75
0.50
0.25
0.00
−0.25
−0.50
−0.75
−1.00
m^3/s^3
−70
−65
−60
−55
−50
−45
−40
−35
−30
Latitude

Figure 7.

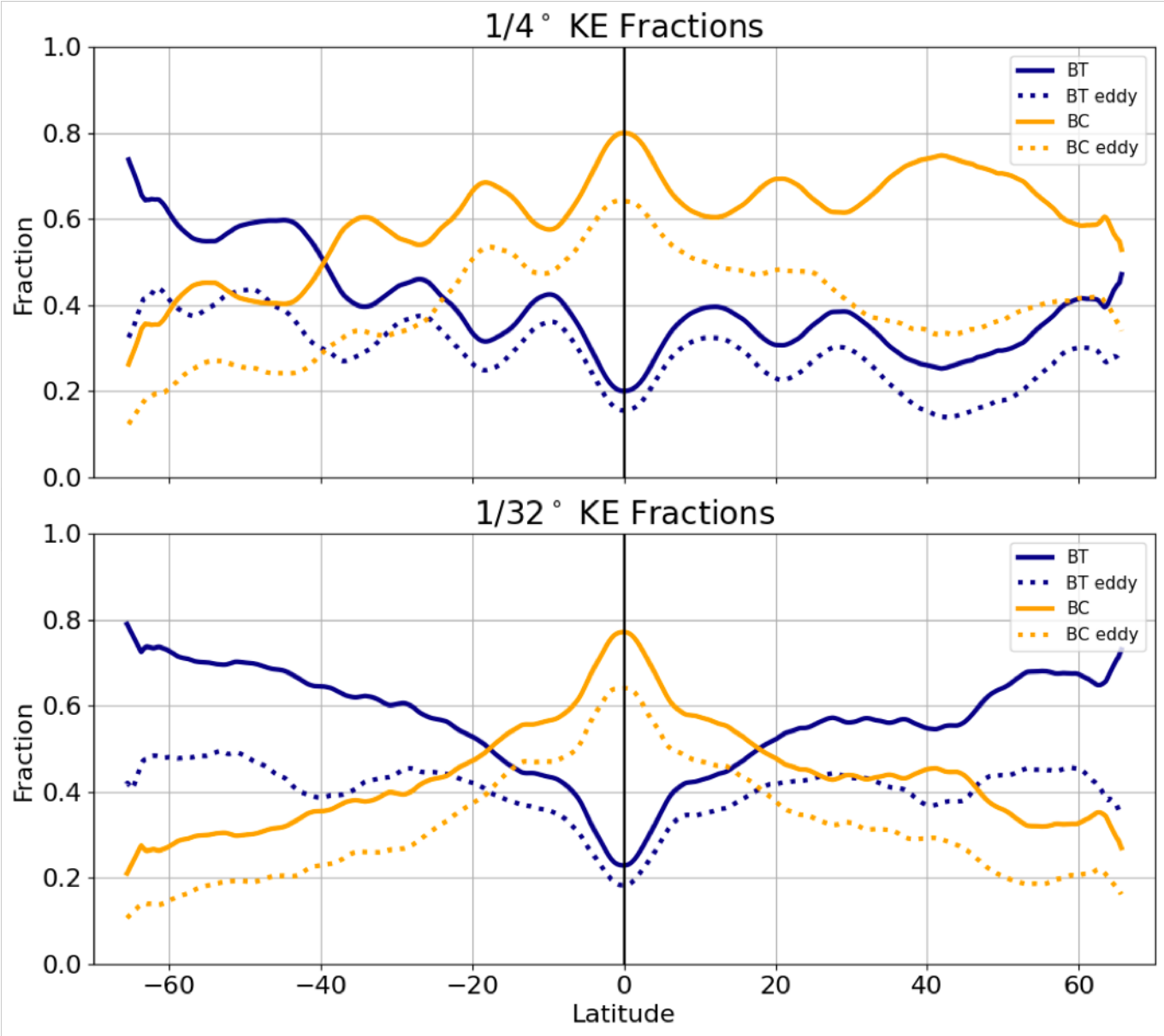
1/4 ° KE Fractions
1/32 ° KE Fractions
BT
BT eddy
BC
BC eddy
Fraction
Latitude
1.0
0.8
0.6
0.4
0.2
0.0
−60
−40
−20
0
20
40
60

Figure 8.

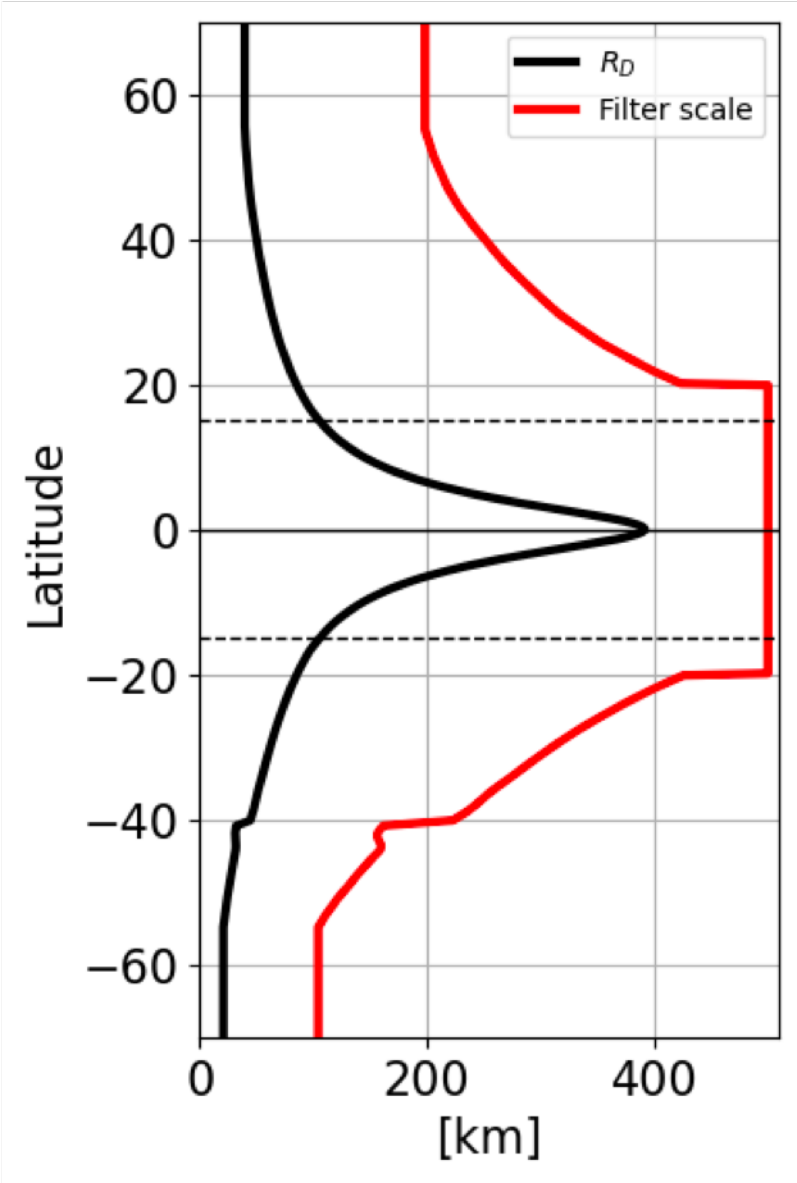
R_D
Filter scale
60
40
20
0
−20
−40
−60
Latitude
0
200
400
[km]

Figure 9.

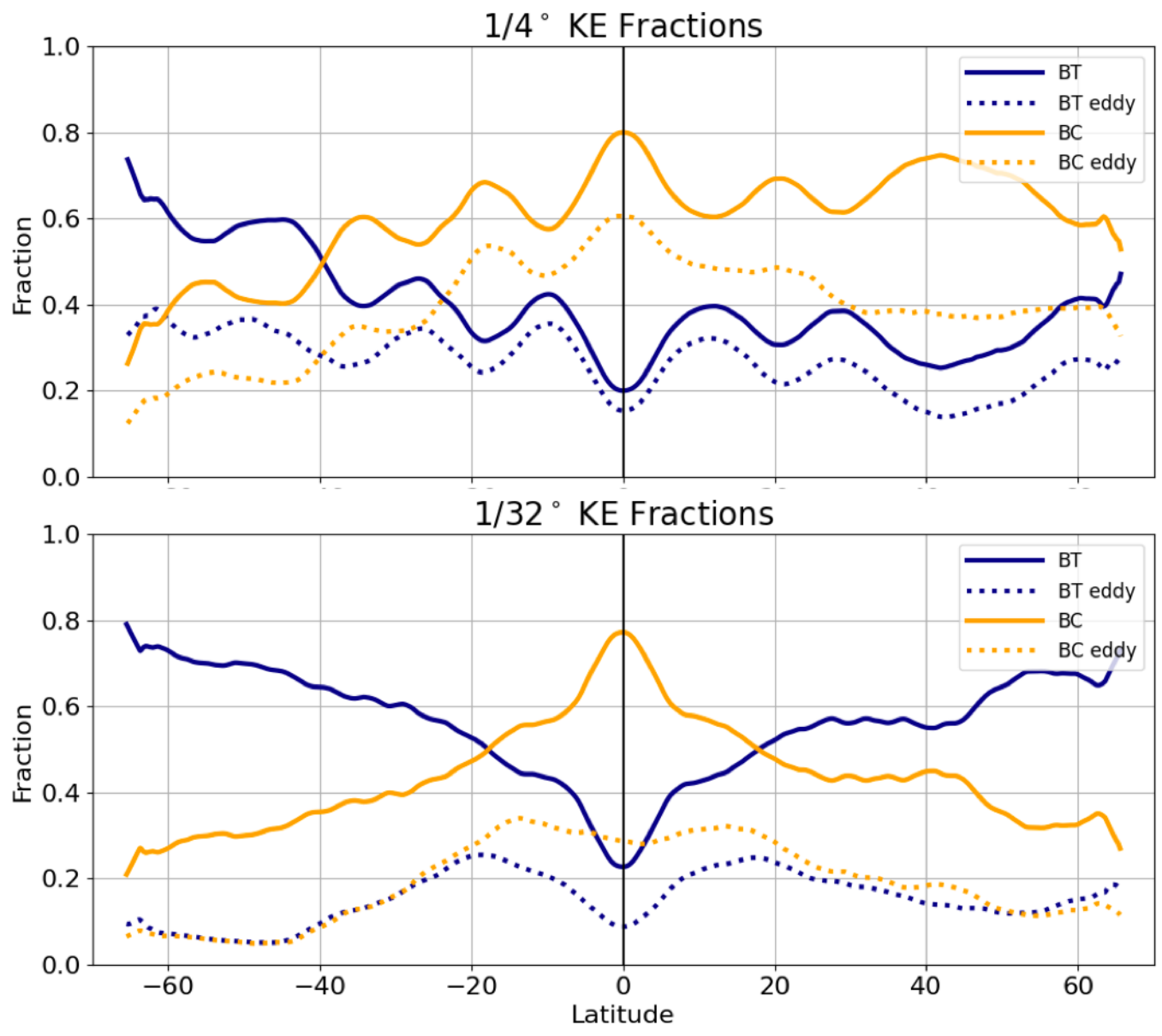
1/4 ° KE Fractions
1/32 ° KE Fractions
BT
BT eddy
BC
BC eddy
Fraction
Latitude
1.0
0.8
0.6
0.4
0.2
0.0
−60
−40
−20
0
20
40
60

Figure 10.

1/4 Degree

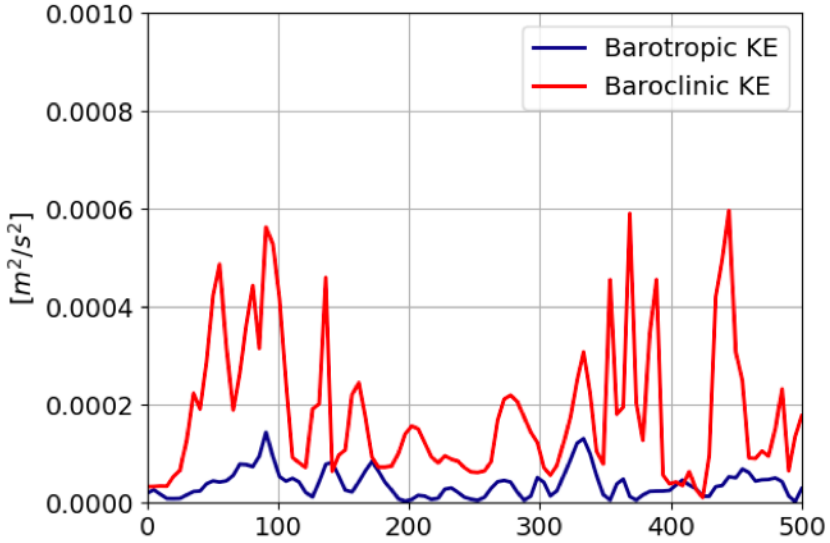

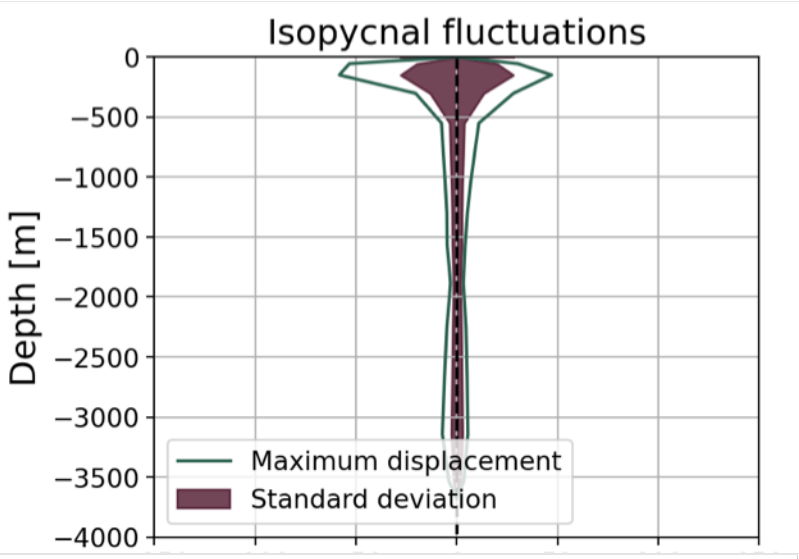

1/32Degree

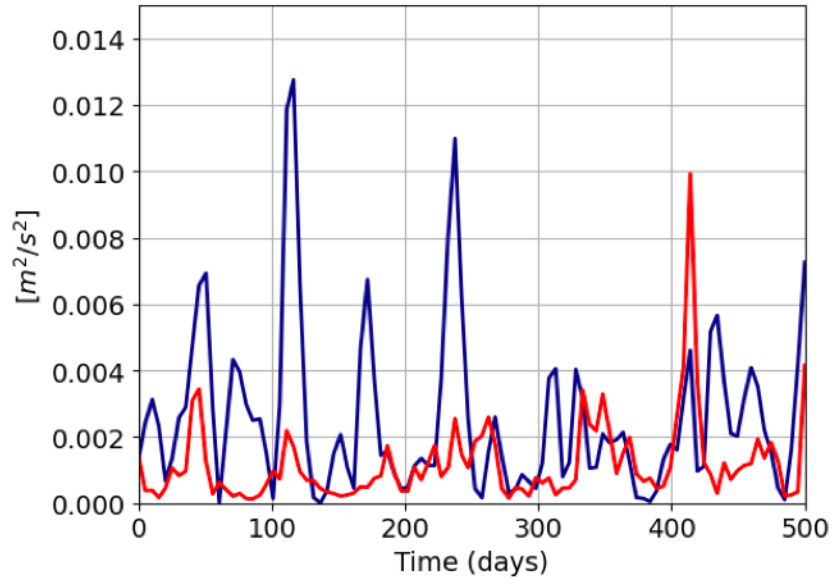

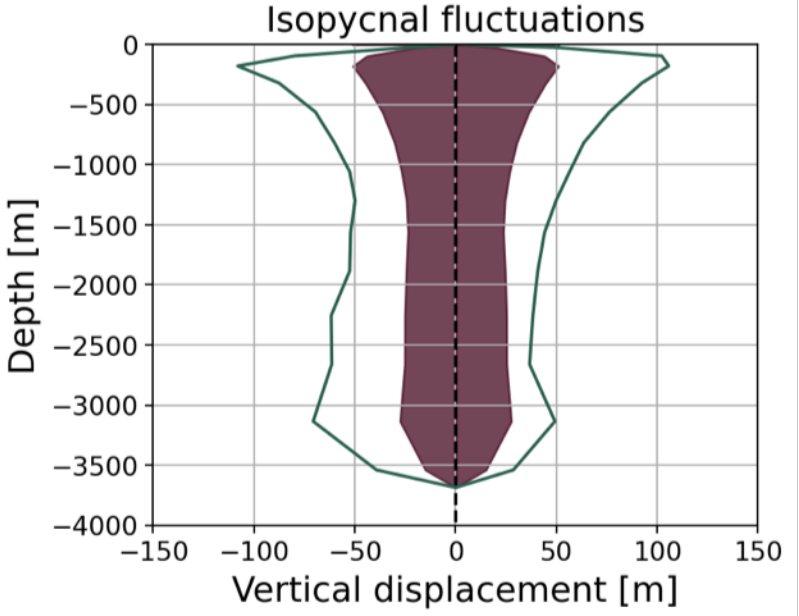

Figure 11.

1/4 Degree

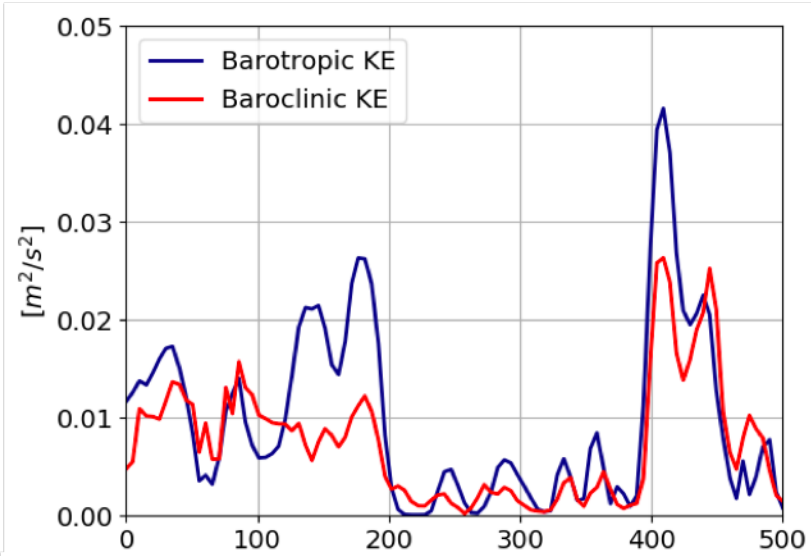

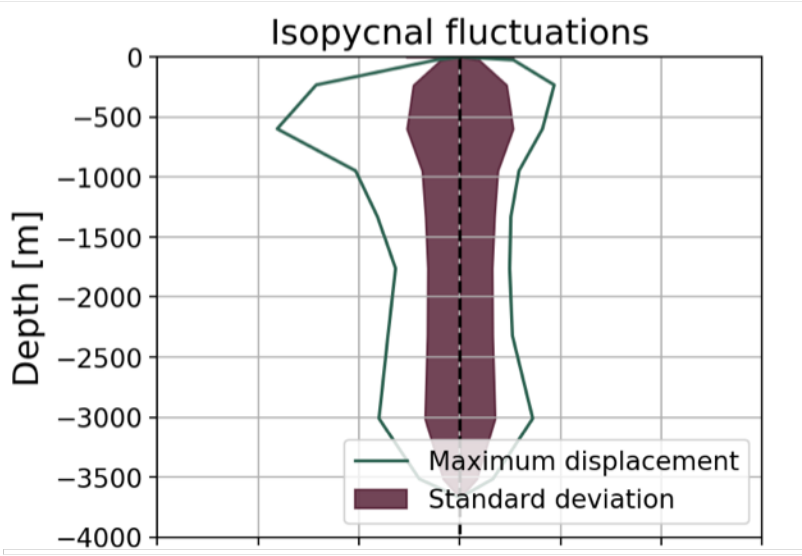

1/32Degree

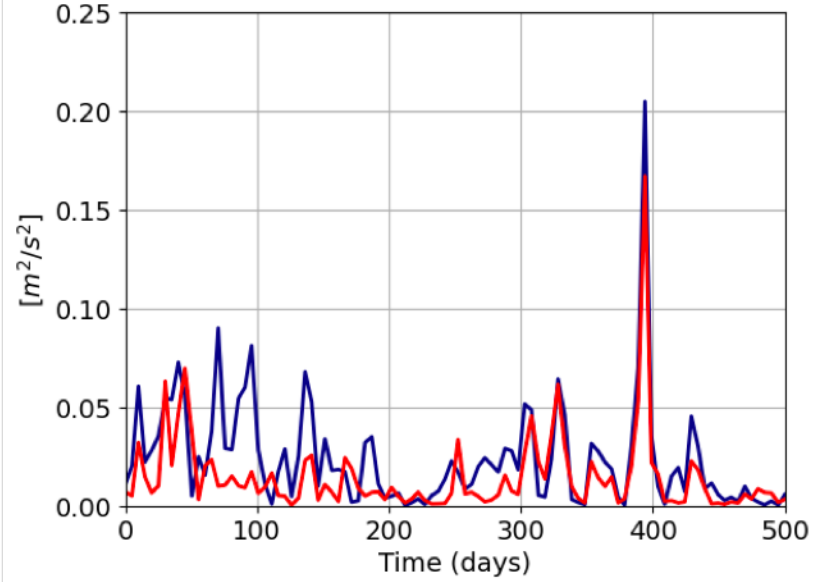

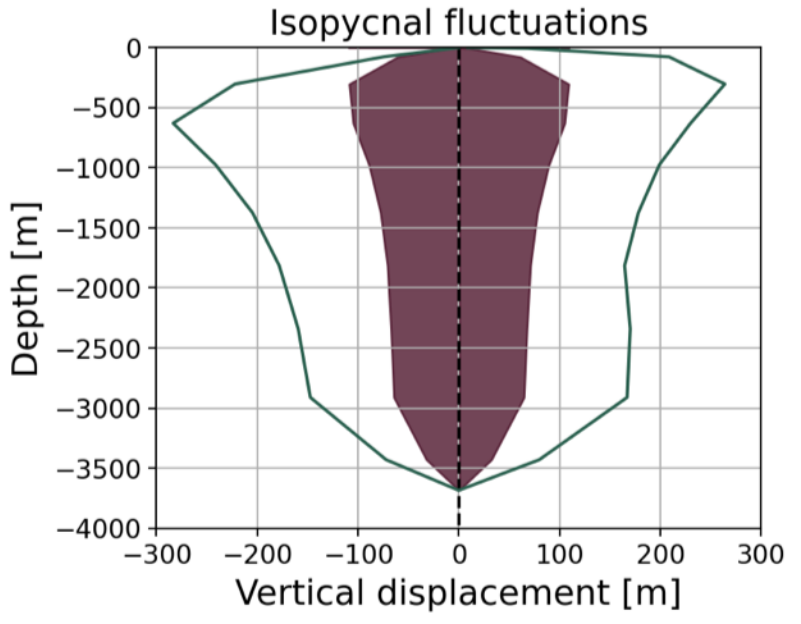

Figure 12.

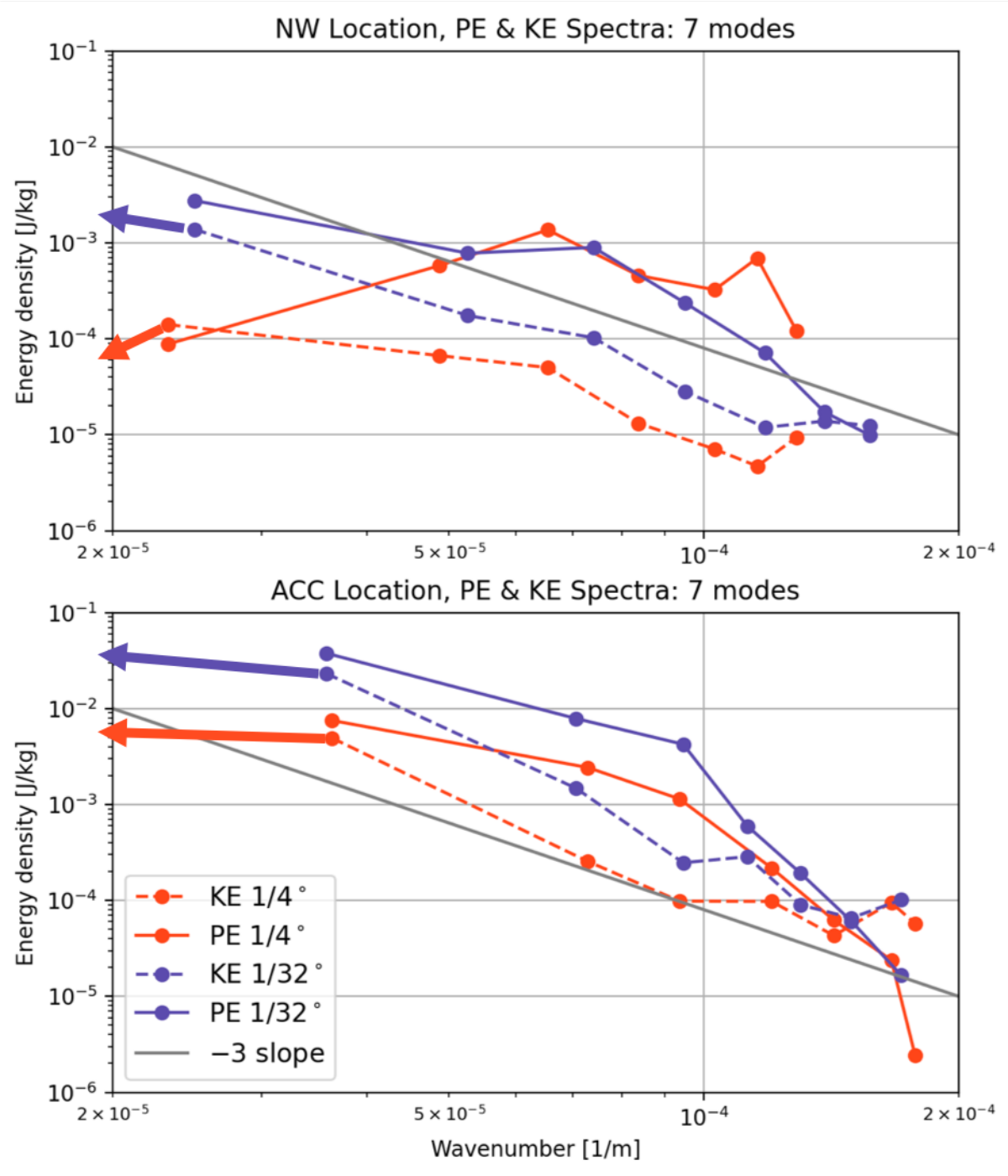
NW Location, PE & KE Spectra: 7 modes
ACC Location, PE & KE Spectra: 7 modes
Energy density [J/kg]
Wavenumber [1/m]
KE 1/4°
PE 1/4°
KE 1/32°
PE 1/32°
−3 slope

Figure 13.

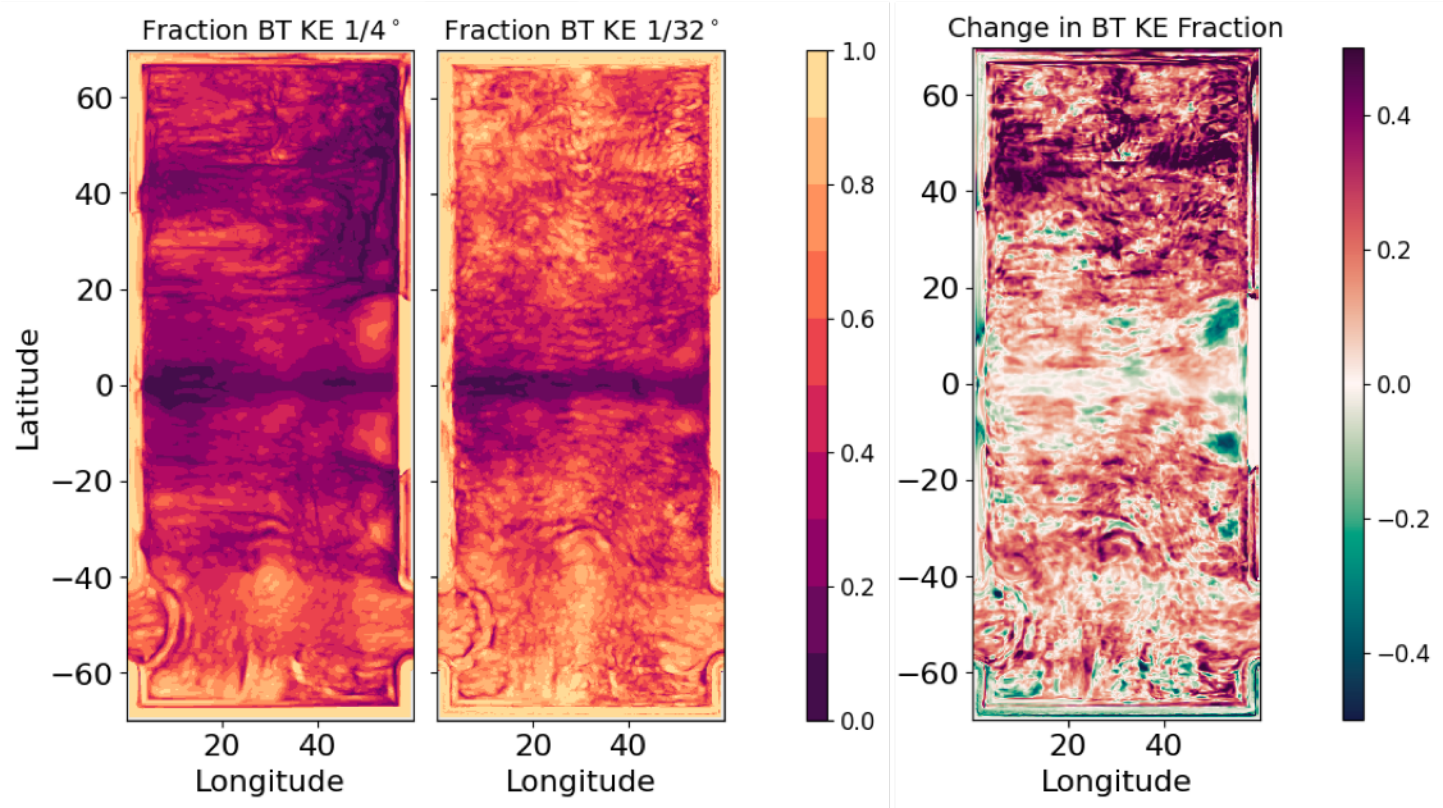
Fraction BT KE 1/4°
Fraction BT KE 1/32°
Change in BT KE Fraction
Latitude
Longitude
Longitude
Longitude
60
40
20
0
−20
−40
−60
20
40
1.0
0.8
0.6
0.4
0.2
0.0
0.4
0.2
0.0
−0.2
−0.4

Figure 14.

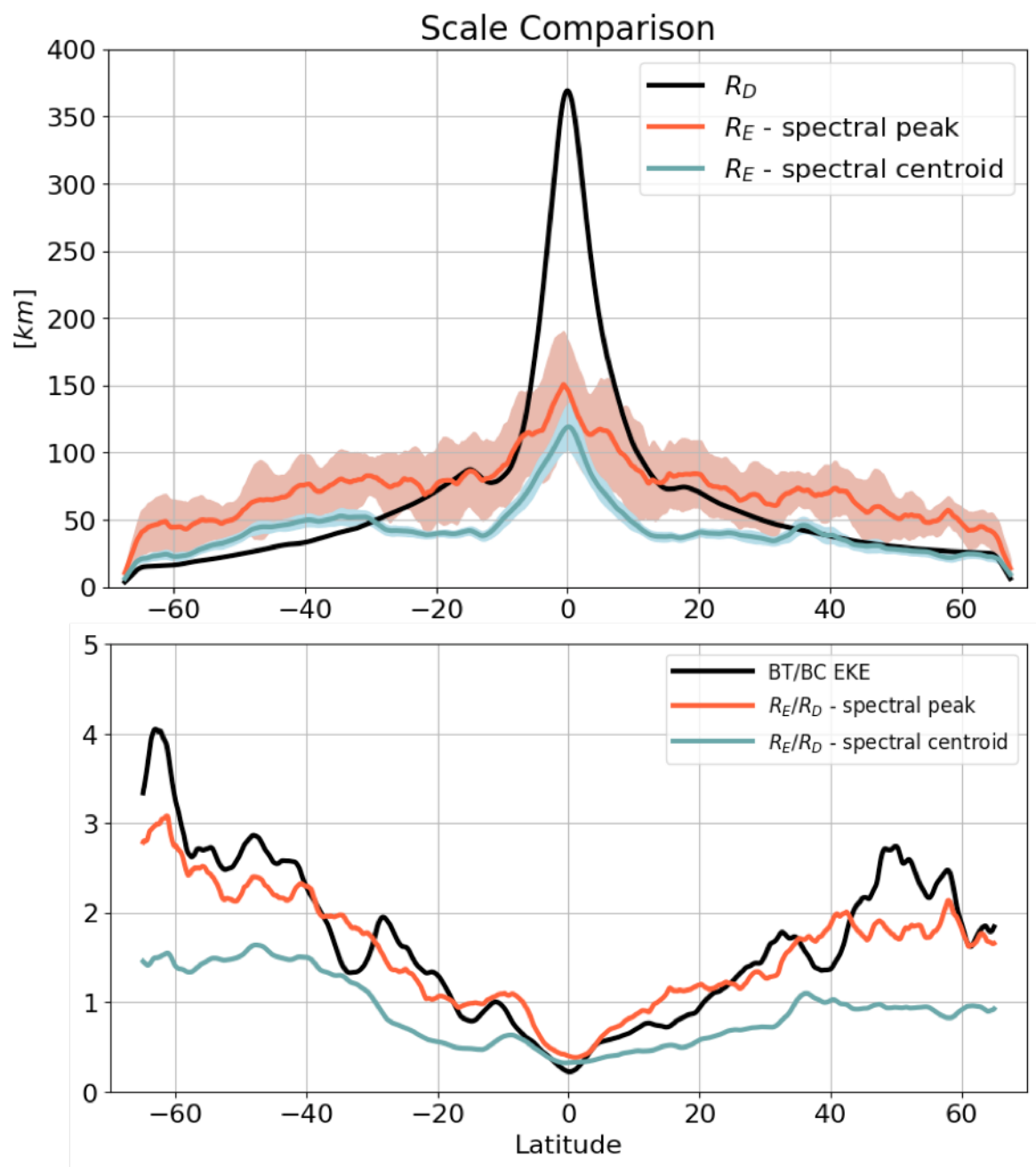
Scale Comparison
R_D
R_E - spectral peak
R_E - spectral centroid
[km]
400
350
300
250
200
150
100
50
0
−60
−40
−20
0
20
40
60
BT/BC EKE
R_E/R_D - spectral peak
R_E/R_D - spectral centroid
5
4
3
2
1
0
Latitude

Figure 15.

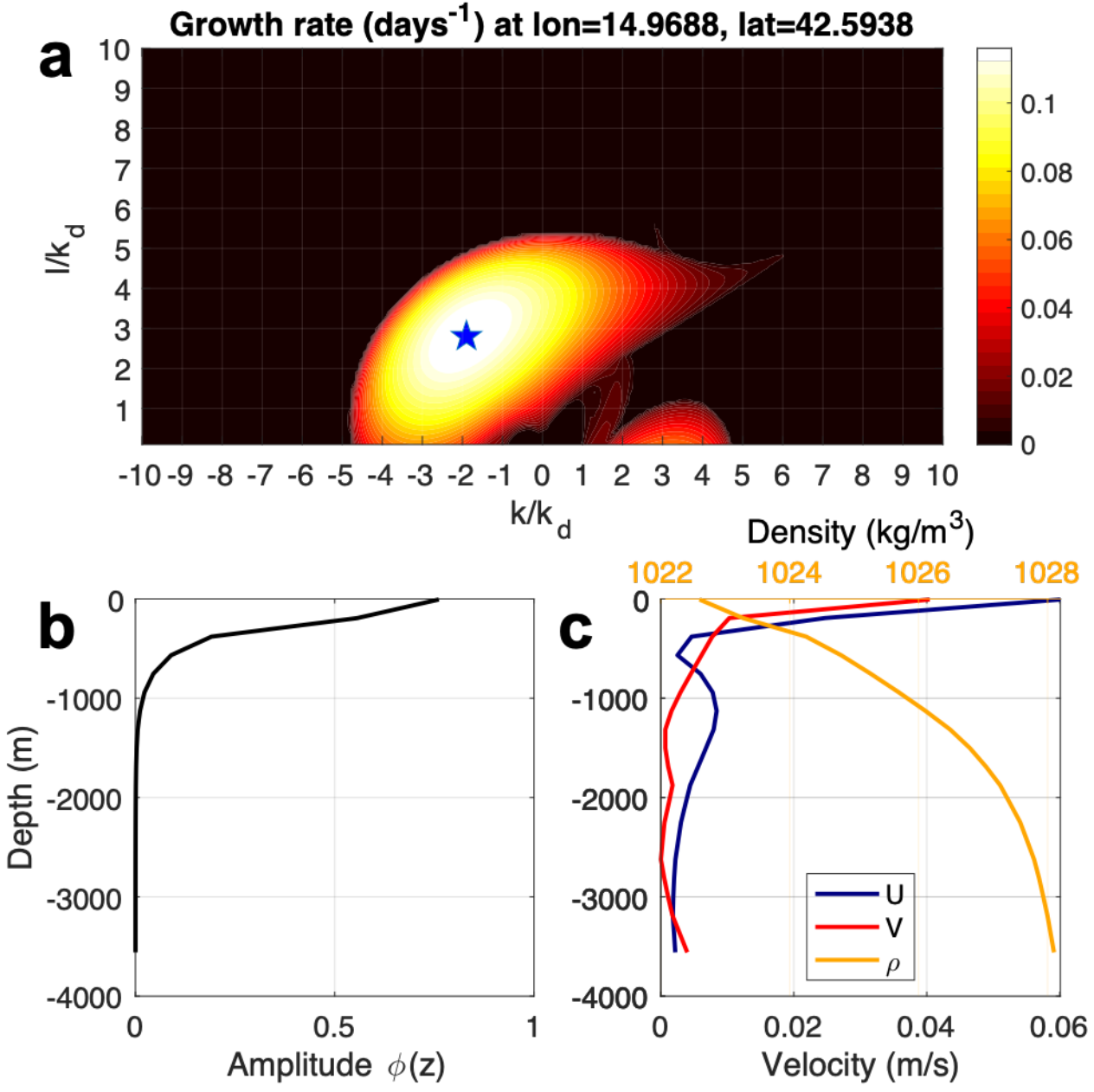
a
Growth rate (days-1) at lon=14.9688, lat=42.5938
l/kd
k/kd
b
Depth (m)
Amplitude ϕ(z)
c
Density (kg/m3)
Velocity (m/s)
U
V
ρ

Figure 16.

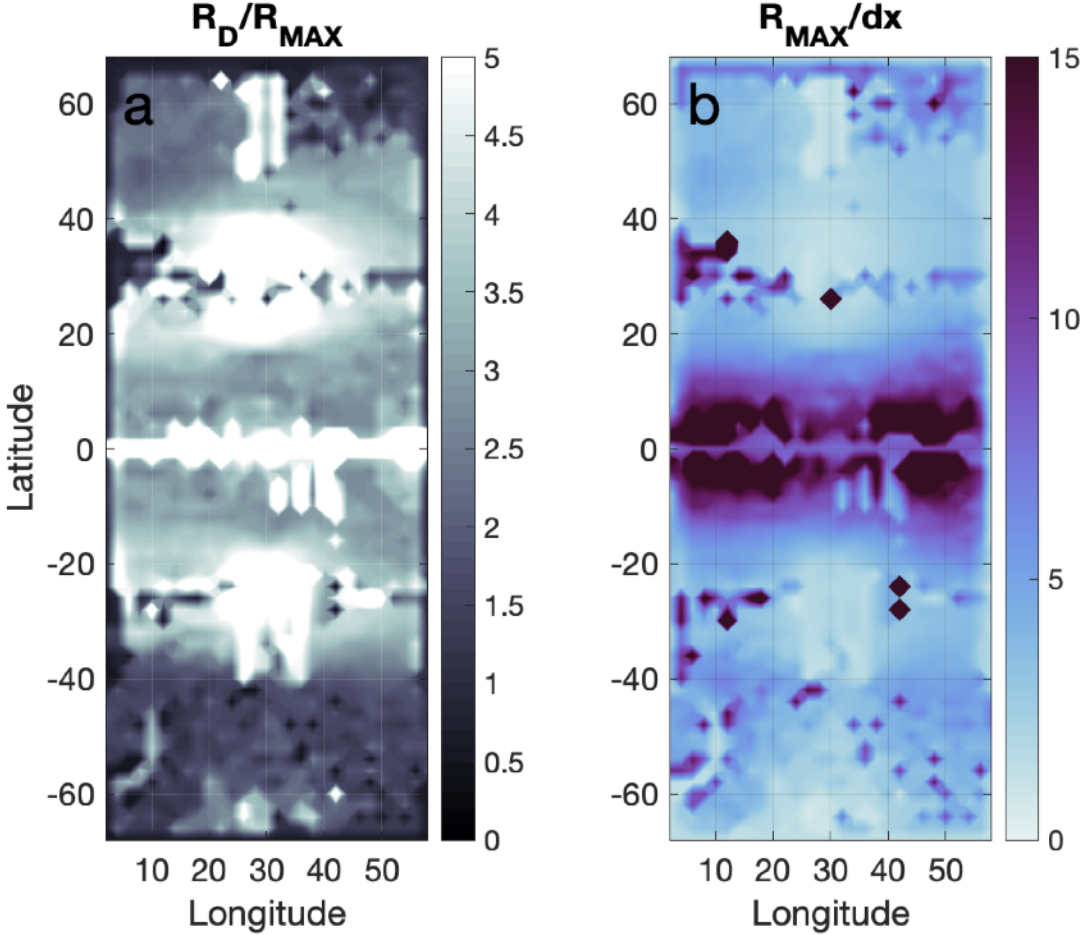
R_D/R_{MAX}
a
60
40
20
0
-20
-40
-60
Latitude
10 20 30 40 50
Longitude
5
4.5
4
3.5
3
2.5
2
1.5
1
0.5
0
R_{MAX}/dx
b
60
40
20
0
-20
-40
-60
10 20 30 40 50
Longitude
15
10
5
0